THE UNIVERSITY OF CHICAGO

MOLECULAR AND COMPUTATIONAL PLATFORMS FOR CANCER DRUG SCREENING AND PRECISION THERAPY

A DISSERTATION SUBMITTED TO
THE FACULTY OF THE PRITZKER SCHOOL OF MOLECULAR ENGINEERING
IN CANDIDACY FOR THE DEGREE OF
DOCTOR OF PHILOSOPHY

BY
JONATHAN MARTIN MATTHEWS

CHICAGO, ILLINOIS
JUNE 2023

TABLE OF CONTENTS

LIST OF FIGURES

ACKNOWLEDGMENTS

The research discussed in this dissertation and my academic, scientific, professional, and personal growth over the course of its progress were made possible, directly and indirectly, by the guidance and vision of my doctoral advisor Professor Savas Tay; the mentorship, hard work, and encouragement of the postdoctoral and senior scientists, research technicians, and fellow graduate students of the Tay Lab; the tether to reality held taut by my closest friends; and everything under the sun from my foundation — Mom and Dad, David, Adam, and Hannah — who have endured and supported me the entire way.

ABSTRACT

Pharmacological cancer therapy can lead to a range of outcomes, even among patients with cancer in the same location, originating from same cell type, and with the same biomolecular markers. Treatment heterogeneity is also reflected at the cellular level, where cells within an individual tumor can exhibit discordant responses to a drug. This fractal nature of cancer diversity has encouraged the development of hundreds of unique drugs and therapeutic regimens, with the ambition of matching each patient to an ideal treatment option. The rich space of possible treatments is infeasible to study *en masse* through clinical trials, motivating the use of disease models to screen and hone in on promising candidates. Drug screening must not only explore the large treatment space, but also extract rich measurements for each condition to reflect nuanced pathophysiological processes. These two aspects often pull experimental designs in opposite directions, constraining assays to explore few conditions in detail (high-content analysis) or many conditions superficially (high-throughput screening).

Here, I describe the development, validation, and exploration of three technologies for high-throughput and high-content drug screening. The first is a deep learning-powered software tool, *OrganoID*, that analyzes microscopy images of patient-derived cancer organoids to follow changes in organoid number, size, and shape in response to drug exposure. The second technology, *PicoScreen*, enables computer-controlled screening of reagent combinations in picoliter droplets with microscopy. Finally, in *Screen-seq*, a novel molecular barcoding and microfluidic strategy measures transcriptomic responses of thousands of individual cells to all possible combinations of multiple reagents under study. These technologies aim to make screening methods more efficient, comprehensive, and information-rich, to expand our understanding of disease processes, such as cancer, and improve treatment options and selection for patients.

CHAPTER 1

INTRODUCTION

Many clinicians and scientists would concede that cancer is an impossible disease to cure. Rather than reflecting a defeatist worldview, this perspective instead gives due credit to the complexity of cancer. Cancer is a disease process characterized by the uncontrolled growth of cells that are no longer constrained by Darwinian obligations to the body as a whole. From this point-of-view, cancerous cells can be considered to have escaped from being parts of a multicellular organism, and instead become more unicellular, boundlessly consuming energy and reproducing as much as possible. Cancer can arise from virtually any type of cell and through innumerable molecular mechanisms. It is understandable, then, that characterizing (and eventually treating) an individual instance of cancer necessitates a equally flexible approach.

Effective cancer treatment hinges on the ability to distinguish malignant cells from non-malignant cells for extermination or removal. For many solid tumors, the distinction can be made almost completely on a spatial basis through surgical excision or radiation therapy focused on the mass and surrounding tissue. Yet for the majority of cancer cases, this approach must be supplemented to completely eliminate the disease. Metastatic disease and blood cancers are not confined to specific locations, delicate anatomical structures and surgical risks may hinder safe resection of solid tumors, and clinical procedures may leave behind residual malignant cells in microscopic margins around the treated region.

Complementary to these approaches are pharmacological treatments – such as chemotherapy, immunotherapy, hormone therapy, and targeted therapy – that chemically induce harmful responses in cancer cells. For example, cytotoxic chemotherapeutic agents block the processes of DNA synthesis and mitosis, which are critical for cancer growth and survival. Many healthy cells, however, also rely on these processes for tissue maintenance and it is this nonspecificity that leads to the adverse effects of chemotherapy. Hair loss, gastrointestinal

damage, a high risk of infection, fatigue, bleeding, and a host of other symptoms are direct and common consequences of chemotherapy. These effects are ameliorated in targeted treatments, which instead use small molecules to interfere with specific receptors and signaling pathways. Similarly, antibody-based therapies recognize particular biomarkers on cancer cells to guide the delivery of cytotoxic drugs or label them for destruction by the immune system. Yet while these modern therapies have considerably improved patient outcomes and quality-of-life, cancer remains, in unfortunately many cases, quite difficult to treat. Many tumors do not exhibit viable molecular targets. Small populations of malignant cells may be less responsive to particular drugs, and can regrow into resistant disease after initial treatment – a process akin to the emergence of antibiotic resistance in bacterial infections.

The molecular differences between healthy and diseased tissue are subtle and heterogeneous, which has prompted the development of hundreds of drug treatments to cover the varieties. Different drugs are often administered together to make treatment more tolerable, effective, and comprehensive. Combination therapies that include drugs with orthogonal mechanisms of action can have a wider therapeutic window, with effects that combine constructively and specifically on diseased cells. Malignant cells may employ several redundant systems for continued growth and survival, which can be disrupted simultaneously through a combination approach. The use of multiple drugs in tandem can also address the challenge of drug resistance, as a cancer cell is putatively less likely to be resistant to several types of drugs at once.

Combination therapy is a powerful strategy to overcome the central limitations of pharmacological cancer treatment, however there are a staggering number of options available, and only some of which might be efficacious for a given patient. These treatments are developed through layers of iterative clinical trials, where components are added to or modified in best-practice regimens and compared for efficacy in randomized groups of patients. However, the full space of treatment possibilities, 2^N in the number of drugs, is clearly infeasible to

explore *en masse* through this approach. As well, the inconsistency in treatment outcomes among patients with seemingly identical cancers has prompted the designation of disease subpopulations, each of which must be studied to identify effective therapies.

High-throughput screening on laboratory models of disease, including cell lines, xenografts, organoids, and cell-free systems, can expedite the exploration process and hone in on promising therapeutic combinations for further investigation. Critical to the design of these assays is the choice of response to be measured. Scalar responses, such as cell growth, necrosis, or metabolic activity, can be easily quantified with molecular dyes and probes; however, these measurements may miss other important endpoints and mechanisms of the drugs under study. As such, high-throughput tools are complemented by high-content analysis, whereby many detailed responses are obtained for a smaller set of conditions. Assay designs must often prioritize either content or throughput, which slows the research cycle.

The research presented in this dissertation largely concerns the design, development, and validation of cancer drug screening tools that help balance content and throughput to examine the detailed effects of multiple treatment conditions on *in vitro* and *ex vivo* disease models. These methods rely heavily on the fields of microfluidics, single-cell sequencing, and deep learning, and I provide a brief background of the relevant topics in Chapter 2. Chapter 3 describes *OrganoID*, a deep-learning software system that analyzes high-throughput organoid experiments to extract high-content morphological measurements. In Chapter 4, I share *PicoScreen*, a microfluidic platform that leverages multiplexed membrane valves to emulsify controlled mixtures of reagents into picoliter droplets, and store the droplets in an ordered grid. Lastly, in Chapter 5, I describe *Screen-seq*, a molecular and microfluidic strategy to efficiently measure the transcriptomic effects that different drug combinations can induce in cancer cells. Together, the resources and results presented in this dissertation contribute to the effort to understand cancer, through its many levels of complexity, and bring effective and tolerable treatments to patients.

CHAPTER 2

TECHNICAL BACKGROUND

2.1 Automated image analysis

A two-dimensonal (2D) computer image is a rectangular grid of *pixels*, where each pixel is an integer or a floating-point (decimal) number. In the most familiar case, the numeric value of each pixel corresponds to a color, so that the image encodes a digitized version of real-world imagery. *Image analysis* aims to extract meaningful information from computer images in order to accomplish a particular task – such as identifying numbers and letters on license plates, object tracking for industrial assembly lines, face recognition on smartphones, and so on. There are many algorithms and computational strategies to automate this process, so that minimal human intervention is required. This section covers a handful of these approaches that are particularly relevant to the research described in Chapter 3.

2.1.1 Image segmentation

A critical step in image analysis is to group pixels that are (or are not) relevant to solving the problem at hand. This step is commonly called image *segmentation*, where a numeric label is assigned to each pixel so that pixels with the same label share an important characteristic or feature. In a chest X-ray photo, for example, pixels that correspond to the heart can be assigned the number 1, pixels that correspond to the lungs can be assigned the number 2, and all other pixels can be assigned the number 0.

The distinction between foreground and background is perhaps the most common image segmentation process, so that superfluous information can be discarded before further analysis. A simple, yet robust, approach is to set a numeric threshold that splits pixel values into foreground and background groups. This threshold can be fixed for the entire image, as determined with approaches such as Otsu's method [1], or can be designed to vary across

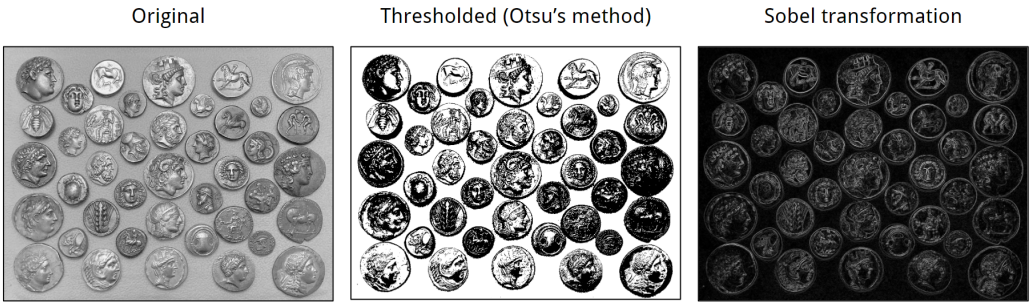

Figure 2.1: Examples of image analysis operations. An image can be thresholded with algorithms such as Otsu's method [1] to distinguish objects, or transformed with convolutional operators, such as with the Sobel edge detector [3], to emphasize or suppress particular features.

the image according to trends in smaller pixel "neighborhoods" [2]. Foreground detection methods in image segmentation produce black-and-white (binary) images, sometimes also called *masks*, where white and black pixels correspond to foreground or background objects (Figure 2.1).

2.1.2 Morpology and transformations

A toolbox of algorithms based on the field of mathematical morphology have been developed to work with binary images and refine the quality of thresholding [4]. Morphological operations sweep a predefined shape (*structuring element*) across the entire image, emphasizing or suppressing regions that match or fail to match the structure. For example, the use of a 7x7 circular structuring element in a binary *erosion* operation will remove white pixels that do not conform to the curvature of a 7-pixel-diameter circle. Conversely, a binary *dilation* operation with the same structuring element will add white pixels in order to fit the contour of a 7-pixel-diameter circle. These steps can be composed together to form a binary *opening* (erosion then dilation) or a binary *closing* (dilation then erosion), which can remove small holes, gaps, or white clusters that do not conform to the structuring element used. Altogether, morphological operations are powerful and flexible methods to refine segmented

images for specific downstream processing tasks.

Mathematical filters and transformations can be applied to images to manipulate and convert representations. The morphological operations discussed above are examples of manipulations within the binary representation of an image, however there is a much broader arsenal of options for image processing. The *distance transformation* operates on a binary image, computing the distance for each black pixel to the nearest white pixel and storing the result in a new decimal-valued image [5]. The *watershed transformation* interprets a grayscale image as a topographical map, identifying the boundaries (ridges) between specific minima (valleys) [6]. The *Hough transformation* identifies specific shapes in an image with a per-pixel voting procedure [7]. An image *convolution* applies a sliding-window filter to groups of pixels, computing the weighted sum for each position. For example, the use of a Gaussian filter will produce a blurred version of the original image. The filters used in the *Sobel transformation* approximate the partial derivatives of an image, to highlight regions with high contrast (edges) [3] (Figure 2.1).

Image transformations are rarely applied in isolation and are instead chained together to form a processing "pipeline" that performs a more general task. A classic example is the Canny edge detector, which uses a Gaussian filter followed by a derivative-estimating convolution (e.g. the Sobel transformation) and then a thresholding operation to produce a binary image that identifies object edges [8]. These edges can be further refined with morphological operations to identify the shapes of individual objects. Image processing pipelines can be constructed iteratively, by selecting operations and parameters by hand to extract the desired information, and offer immense flexibility to solve diverse sets of problems.

2.1.3 Convolutional neural networks

Convolution transformations are particularly powerful and flexible tools in image processing, and the choice of filter can have a wide range of effects on the resulting image. Furthermore,

as each filter can take on any value and be composed together in any order, there is an effectively infinite number of possibilities to use. Machine learning algorithms can be used to optimize convolution-based image processing pipelines to both produce results that closely match handcrafted examples and generalize to new sets of data. A convolutional neural network is an image processing pipeline that relies on several layers of convolution operations, but extends these with additional pipeline steps that can capture nonlinear features (recall that a convolution is effectively a weighted sum, or *linear combination* of an image) [9]. For example, a nonlinear *activation function* is applied to the results of each operation before continuing forward in the pipeline.

Training a convolutional neural network refers to the process of optimizing the parameters of each convolutional layer to minimize a *loss function*, which is designed to produce a continuously differentiable metric of the model's performance. The partial differentiability of this function is criticial to determine the direction and magnitude of parameter updates that will improve the model (the *gradient*). While optimization on a closed-form differentiable function is analytically straightforward, convolutional neural networks are often functions of thousands or millions of arguments with no closed-form expression. Data sets similarly must contain thousands or millions of examples, each of which must be evaluated through the differentiated loss function to compute the gradient. Furthermore, the loss function will often have many local minima or saddle points across the model configuration space, which can "trap" solutions in suboptimal states. Accordingly, many network training methods (sometimes called *optimizers*) have been developed as variants of *stochastic* gradient descent algorithms, which can estimate the high-dimensional gradient with low computational burden and escape small local optima or saddle points [9, 10]. The starting configuration of network parameters can also have a profound impact on the converged solution, and various strategies have been developed here, too, to initialize and sample from several likely positions.

Because a convolutional neural network needs to be trained on example images, it is

quite likely that, at a certain point, the model begins to prioritize performance on the specific examples rather than the problem as a whole. This phenomenon is called *overfitting*, and can be intuitively understood as the model "memorizing" the training data. To combat overfitting, the dataset of examples is typically split into two groups – one to use for the mathematical optimization process (the *training dataset*), and the other to monitor performance on new examples (the *validation dataset*). Early in the training process, performance on both datasets should comparable, albeit moderate. However, as the network becomes more and more optimized for the training dataset, it will produce comparatively worse results for the validation dataset. When this junction is detected, the training process should be stopped and finalized, as further optimization will only produce a model that is more fit to the specific examples. Complementary strategies, such as model structure and simplification, dropout layers [11], or regularization penalties [12], can be used to additionally limit overfitting. Lastly, the design of a machine learning pipeline will likely go through several iterations as the data scientist hones in on an ideal configuration. The number of convolution operations, the size of each update during gradient descent, and the selection of regularization strategies are all examples of *hyperparameters* – properties of the model that are not optimized by the learning algorithm, but by the designer themself. As such, these hyperparameters are also subject to the risks of overfitting and must be evaluated with yet another independent dataset (the testing dataset) that, once used, restricts further modifications to the model [13].

2.2 Microfluidics

The field of microfluidics is, perhaps obviously, characterized by the manipulation of small volumes of fluid. This discipline is important for a range of applications, from chemical synthesis to inkjet printing, but is particularly relevant to cellular and molecular biology, which are inherently concerned with microscopic phenomena. Microfluidic devices (or "chips") are

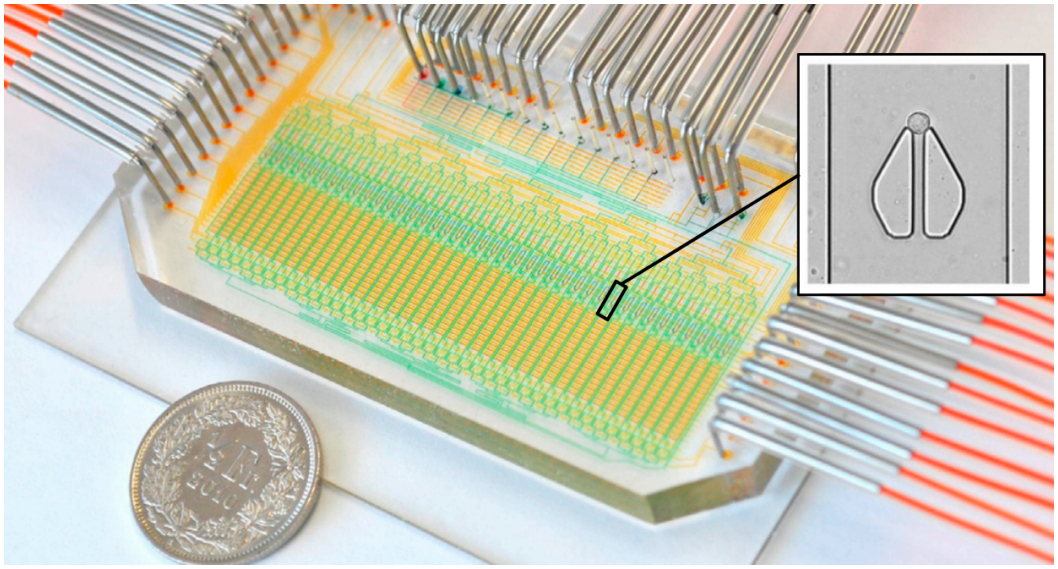

Figure 2.2: A microfluidic device. Microfluidic devices contain micron-scale embedded channels and chambers to manipulate fluids. Cells can be cultured on these devices for analysis with microscopy (shown in inset). Adapted from [18] with permission.

fabricated to contain embedded channels, chambers, pumps, and other functional elements [14, 15] (Figure 2.2) – just as electronic devices are built from conductive wiring, capacitors, batteries, and so on. These devices can be loaded with cells, signaling molecules, drugs, or other organic substances to study and manipulate small-scale biological systems [16]. For example, next-generation sequencing platforms use microfluidic devices (called *flow cells*) to capture DNA fragments and automate the steps of sequencing-by-synthesis [17]. This section describes several important aspects of microfluidics that are heavily involved in the work of Chapter 4 and Chapter 5.

2.2.1 Device fabrication

Microfluidic devices can be fabricated from polydimethylsiloxane (PDMS), a transparent silicone polymer that is non-toxic to cells [16]. PDMS is commonly derived from a viscous liquid of monomers that, when mixed with a crosslinking reagent and heated, solidifies to

form a flexible solid. A versatile strategy for PDMS device fabrication is *soft lithography*, in which the viscous PDMS is poured on top of a mold, or relief, of the device to be fabricated [19]. The PDMS is cured on the mold and then peeled off, retaining the negative relief, and the mold can then be reused to produce more PDMS-based devices. At this stage, millimeter pinholes are typically punched out of the device for later connections to external tubing.

The grooves in the PDMS slab formed from soft lithography will act as the "ceiling" and "walls" of microfluidic channels; however, the slab must be bonded to a separate surface that will form the channel "floor" and seal the device. This substrate is typically borosilicate glass, however PDMS can also be bonded to plastics, metals, or even other slabs of PDMS. Among several bonding methods that can be used, such as thermal or chemical bonding, *plasma bonding* is a particularly robust and effective process [20]. In plasma bonding, the PDMS device and bonding substrate are placed in a vacuum chamber, which is evacuated and then filled with pure oxygen gas. An electromagnetic coil is then activated to ionize the oxygen and form a plasma, which attacks the substrates in the chamber to form reactive groups, such as hydroxyls and free radicals. By pressing the activated surfaces together, covalent bonds will form, permanently sealing the final device.

Through soft lithography, PDMS will closely conform to the shape of the designed mold. As such, the precision of a microfluidic device is largely determined by the mold fabrication process. Microfluidic molds are typically fabricated, in turn, by photolithography procedures borrowed from the semiconductor industry [21]. In photolithograpy, a light-reactive viscous liquid (called a *photoresist*) is spun onto a silicon wafer at a high speed to form a uniform layer of sub-millimeter thinness. When a "negative" photoresist is exposed to light of a particular wavelength, it will crosslink together into a rigid solid. The unreacted photoresist can then be dissolved and washed off of the wafer. In contrast, a "positive" photoresist weakens upon exposure for easy removal by the appropriate solvent. By exposing the coated wafer to a masked or rasterized laser pattern and "developing" the wafer in a solvent,

micron-resolution features can be produced on a silicon wafer in solidified photoresist. In semiconductor fabrication, these photoresist patterns are typically used to resist the action of harsh etching agents (hence the name), which engrave the pattern in the wafer. In soft lithography, however, these photoresists are used as the relief themselves for the final mold.

2.2.2 Droplet microfluidics

Microfluidic devices can be used to isolate individual cells, which makes them especially useful for single-cell analysis [22, 23]. In droplet-based microfluidic devices, a flowing channel of cells in media converges on a channel that contains oil, which generates a stream of identical droplets at the junction of the immiscible fluids. Each droplet serves as a self-contained reaction vessel, isolated from its neighbors, analogous to the wells of a microtiter plate. Moreover, if the sample of cells is made sufficiently dilute, most droplets will be empty, a few will contain a single cell, and virtually none will contain more than one cell [24]. This phenomena is well-defined, closely following the Poisson distribution for independent events with a known mean (the concentration of cells divided by the volume of each droplet). Perhaps most impressively, droplets can be stably generated at kilohertz rates, producing hundreds of independent cell-containing chambers per second [25]. The throughput that is possible with droplet microfluidics makes it an indispensable tool for cellular and biomolecular research.

2.2.3 Membrane valves

Microfluidic devices can also be designed with integrated valves to precisely control the flow of reagents [26]. To form a microfluidic valve, two flat layers of PDMS with embedded microchannels are stacked on top of one another and bonded together. In this architecture, the ceiling of one channel serves as the floor of the other – a thin membrane of PDMS that separates the the two. The PDMS membrane is highly flexible, and can be deflected in either direction based on the pressure difference of the two channels. Typically, the channels

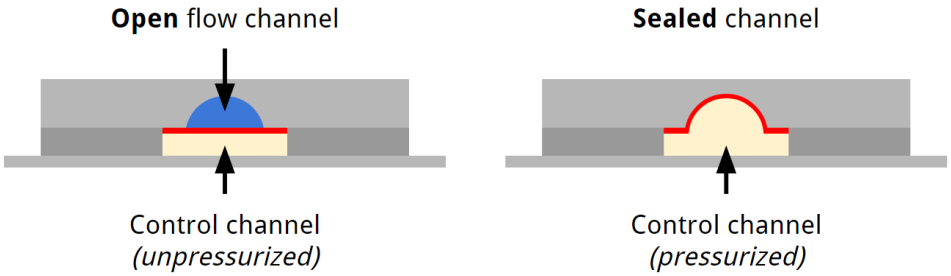

Figure 2.3: A microfluidic membrane valve. Valves can be integrated into microfluidic devices with two-layer soft lithograpy. A thin membrane of PDMS (red) is fabricated between two bonded channels, one for the flow of reagents (blue), and the other for valve control (beige). The membrane can be deflected into either channel based on the difference in pressure, forming a reversible seal. The flow channel at the valve intersection is designed to have a rounded cross-section to ensure complete valve closure.

in one layer are designated for the flow of reagents (flow channels), while channels in the other are used to control the pressure difference across the membrane (control channels). By applying a high pressure to a channel of the controlling layer, the membrane will be reversibly deformed to completely seal the opposing channel, functioning as a microfluidic valve (Figure 2.3).

Membrane valves are powerful building blocks that can be used to pump, mix, and route reagents to specific channels and chambers on a microfluidic chip [15, 27]. Valve actuation can be achieved by hand, such as compressing a syringe of air connected to each valve channel. Alternatively, external electronic solenoids can be used to actuate pressurization under the control of computer software to automatically carry out programmed experiments and operations.

The arrangement of valves in a microfluidic chip can be configured to perform tasks beyond control of flow in a single channel. Multiple valves can be chained together across one channel and actuated in a specific sequence to pump fluids at accurate volumetric flow rates through peristalsis [27]. A single valve can also span many channels, effectively "multiplexing" the valve control signal to manipulate multiple channels at once [15]. By combining

several multiplexed valves together, a large number of flow channels can be addressed with far fewer control channels.

2.3 Single-cell transcriptomics

The phenotype of a cell describes its behavior amidst a busy environment of chemicals, radiation, and other forms of stimuli. By definition, cells with different phenotypes exhibit different responses to the same condition. Phenotypes are not fixed over the lifetime of a cell, and the term "cell state" is often used to capture this dynamic quality [28–30]. The state of a cell determines if it should secrete cytokines, divide uncontrollably, or undergo programmed death. Cell state is determined by functional elements, such as proteins or non-coding RNA, that drive cellular behaviors and responses. The responsibilities of proteins in cellular activity and maintenance have been particularly well-characterized, such as signal transduction, scaffolding, and metabolism [31–33]. As such, the composition of proteins that are expressed in a cell is one useful description of its overall state. Upstream of protein production and regulation is messenger RNA (mRNA), so-named as the intermediate component facilitating information exchange from the genome to the ribosome. While mRNA is one degree further from cellular activities than proteins, it contains a consistent and distinct structure, namely the polyadenylated (poly-A) region at its tail end, that makes it much easier to capture, purify, and measure [34]. The set of mRNA molecules in a cell is referred to here as the cellular *transcriptome*, and is another useful way to characterize the state, and hence phenotype, of a cell [35–37].

There are several methods to measure the transcriptome [35, 37, 38]. Biased approaches, such as cDNA microarrays, use synthetic oligonucleotide probes to quantify the abundance of specific mRNA molecules that contain known complementary sequences. In contrast, RNA sequencing directly detects the sequence of nucleotides present in a sample, without requiring any prior knowledge of the genome. Sequencing can provide more precise, flexible,

and comprehensive transcriptomic measurements [34], including the detection of unforeseen alternatively spliced transcripts [39]. In mRNA sequencing, substrate-attached polythymidine (poly-T) oligomers are used to bind to the poly-A tail of mRNA molecules, so that they can then be chemically or magnetically purified from any non-messenger RNA in the sample [40]. Viral reverse transcriptases (RT) convert the captured RNA to more stable cDNA, which can then be amplified through polymerase chain reaction (PCR) – a process together referred to as RT-PCR. Finally, the amplified products are fragmented and analyzed through standard DNA sequencing methods.

In bulk RNA sequencing, the mRNA from many cells is collected and sequenced together, which can be useful to characterize transcriptomic features shared among cells in a particular tissue. However, as discussed, cellular behaviors can vary even among cells from the same tissue or of the same histological type; these phenomena are obscured in bulk assays, which produce population-averaged measurements [41–43]. This limitation has motivated the development of single-cell RNA sequencing technologies (scRNA-seq) to reveal the heterogeneous states of individual cells. Many of the first scRNA-seq methods to be developed rely on cell sorters to distribute individual cells into separate wells of a microplate [44–47]. In these approaches, each well is also loaded with a unique PCR primer and amplified in parallel, so that the cDNA sequences of released mRNA molecules are appended to an oligonucleotide "barcode" that corresponds to a single well and, hence, a single cell. The amplified molecules are then pooled and sequenced together as in bulk methods; however, now each cDNA read is accompanied by its molecular barcode, which can be used to group reads together and assemble the transcriptome for each cell.

Plate-based scRNA-seq methods can measure hundreds of cells in an assay, however even this is thousands of times less than the number of cells in a cubic millimeter of tissue. As such, rare cell types may be lost among the majority and not captured due to limited scalability of well plates and microliter pipetting. These limitations have encouraged the

integration of other experimental strategies, such as droplet microfluidics [22, 23], to reach higher orders of magnitude in single-cell assays. In droplet sequencing, each cell is isolated in an individual droplet that contains membrane-lysing reagents and a microscopic bead coated with poly-T oligomers to capture the released mRNA [48, 49]. The oligomers also contain a region with a nucleotide sequence that is unique to each bead, as well as a universal primer sequence for mRNA amplification with RT-PCR. Through this strategy, the resulting cDNA molecules will include a sequence (a molecular *barcode*) that is shared only with other molecules amplified from the same bead. The cDNA library can now be pooled and sequenced in bulk. Because virtually no droplets contain more than one cell, reads that contain the same molecular barcode can be confidently assumed to have come from the the same single cell [24].

2.4 References

1. Bangare, S. L., Dubal, A., Bangare, P. S. & Patil, S. Reviewing Otsu's Method For Image Thresholding. en. *International Journal of Applied Engineering Research* **10,** 21777–21783. ISSN: 0973-4562, 0973-9769. `http://ripublication.com/ijaerdoi/2015/ijaerv10n9_20.pdf` (2023) (May 2015).

2. Singh, T. R., Roy, S., Singh, O. I., Sinam, T. & Singh, K. M. *A New Local Adaptive Thresholding Technique in Binarization* arXiv:1201.5227 [cs]. Jan. 2012. `http://arxiv.org/abs/1201.5227` (2023).

3. Sobel, I. An Isotropic 3x3 Image Gradient Operator. *Presentation at Stanford A.I. Project 1968* (Feb. 2014).

4. Chanda, B. Morphological Algorithms for Image Processing. *IETE Technical Review* **25,** 9–18. ISSN: 0256-4602. (2023) (Jan. 2008).

5. Breu, H., Gil, J., Kirkpatrick, D. & Werman, M. Linear time Euclidean distance transform algorithms. *IEEE Transactions on Pattern Analysis and Machine Intelligence* **17.** Conference Name: IEEE Transactions on Pattern Analysis and Machine Intelligence, 529–533. ISSN: 1939-3539 (May 1995).

6. Roerdink, J. B. & Meijster, A. The Watershed Transform: Definitions, Algorithms and Parallelization Strategies. *Fundamenta Informaticae* **41,** 187–228. ISSN: 01692968. https://www.medra.org/servlet/aliasResolver?alias=iospress&doi=10.3233/FI-2000-411207 (2022) (2000).

7. Illingworth, J. & Kittler, J. A survey of the hough transform. en. *Computer Vision, Graphics, and Image Processing* **44,** 87–116. ISSN: 0734-189X. https://www.sciencedirect.com/science/article/pii/S0734189X88800331 (2023) (Oct. 1988).

8. Canny, J. A Computational Approach to Edge Detection. *IEEE Transactions on Pattern Analysis and Machine Intelligence* **PAMI-8.** Publisher: Institute of Electrical and Electronics Engineers (IEEE), 679–698. ISSN: 0162-8828. http://dx.doi.org/10.1109/tpami.1986.4767851 (Nov. 1986).

9. Gu, J. *et al.* Recent advances in convolutional neural networks. en. *Pattern Recognition* **77,** 354–377. ISSN: 0031-3203. https://www.sciencedirect.com/science/article/pii/S0031320317304120 (2023) (May 2018).

10. Kingma, D. P. & Ba, J. Adam: A Method for Stochastic Optimization. Publisher: arXiv Version Number: 9. https://arxiv.org/abs/1412.6980 (2022) (2014).

11. Baldi, P. & Sadowski, P. J. *Understanding Dropout* in *Advances in Neural Information Processing Systems* **26** (Curran Associates, Inc., 2013). https://proceedings.neurips.cc/paper/2013/hash/71f6278d140af599e06ad9bf1ba03cb0-Abstract.html (2023).

12. Pereyra, G., Tucker, G., Chorowski, J., Kaiser, Ł. & Hinton, G. Regularizing Neural Networks by Penalizing Confident Output Distributions. Publisher: arXiv Version Number: 1. https://arxiv.org/abs/1701.06548 (2023) (2017).

13. Ying, X. An Overview of Overfitting and its Solutions. en. *Journal of Physics: Conference Series* **1168.** Publisher: IOP Publishing, 022022. ISSN: 1742-6596. https://doi.org/10.1088/1742-6596/1168/2/022022 (2023) (Feb. 2019).

14. Whitesides, G. M. The origins and the future of microfluidics. en. *Nature* **442.** Number: 7101 Publisher: Nature Publishing Group, 368–373. ISSN: 1476-4687. https://www.nature.com/articles/nature05058 (2023) (July 2006).

15. Melin, J. & Quake, S. R. Microfluidic Large-Scale Integration: The Evolution of Design Rules for Biological Automation. *Annual Review of Biophysics and Biomolecular Structure* **36.** _eprint: https://doi.org/10.1146/annurev.biophys.36.040306.132646, 213–231. https://doi.org/10.1146/annurev.biophys.36.040306.132646 (2023) (2007).

16. Banik, S. *et al.* The revolution of PDMS microfluidics in cellular biology. *Critical Reviews in Biotechnology* **43,** 465–483. ISSN: 0738-8551. https://doi.org/10.1080/07388551.2022.2034733 (2023) (Apr. 2023).

17. Hu, T., Chitnis, N., Monos, D. & Dinh, A. Next-generation sequencing technologies: An overview. en. *Human Immunology. Next Generation Sequencing and its Application to Medical Laboratory Immunology* **82,** 801–811. ISSN: 0198-8859. https://www.sciencedirect.com/science/article/pii/S0198885921000628 (2023) (Nov. 2021).

18. Junkin, M. *et al.* High-Content Quantification of Single-Cell Immune Dynamics. English. *Cell Reports* **15.** Publisher: Elsevier, 411–422. ISSN: 2211-1247. https://www.cell.com/cell-reports/abstract/S2211-1247(16)30289-3 (2023) (Apr. 2016).

19. Rogers, J. A. & Nuzzo, R. G. Recent progress in soft lithography. en. *Materials Today* **8,** 50–56. ISSN: 1369-7021. https://www.sciencedirect.com/science/article/pii/S1369702105007029 (2023) (Feb. 2005).

20. Borók, A., Laboda, K. & Bonyár, A. PDMS Bonding Technologies for Microfluidic Applications: A Review. en. *Biosensors* **11.** Number: 8 Publisher: Multidisciplinary Digital Publishing Institute, 292. ISSN: 2079-6374. https://www.mdpi.com/2079-6374/11/8/292 (2023) (Aug. 2021).

21. McDonald, J. C. *et al.* Fabrication of microfluidic systems in poly(dimethylsiloxane). en. *ELECTROPHORESIS* **21,** 27–40. ISSN: 1522-2683. https://onlinelibrary.wiley.com/doi/abs/10.1002/%28SICI%291522-2683%2820000101%2921%3A1%3C27%3A%3AAID-ELPS27%3E3.0.CO%3B2-C (2023) (2000).

22. Shang, L., Cheng, Y. & Zhao, Y. Emerging Droplet Microfluidics. *Chemical Reviews* **117.** Publisher: American Chemical Society, 7964–8040. ISSN: 0009-2665. https://doi.org/10.1021/acs.chemrev.6b00848 (2023) (June 2017).

23. Joensson, H. N. & Andersson Svahn, H. Droplet Microfluidics—A Tool for Single-Cell Analysis. en. *Angewandte Chemie International Edition* **51,** 12176–12192. ISSN: 1521-3773. https://onlinelibrary.wiley.com/doi/abs/10.1002/anie.201200460 (2023) (2012).

24. J. Collins, D., Neild, A., deMello, A., Liu, A.-Q. & Ai, Y. The Poisson distribution and beyond: methods for microfluidic droplet production and single cell encapsulation. en. *Lab on a Chip* **15.** Publisher: Royal Society of Chemistry, 3439–3459. https://pubs.rsc.org/en/content/articlelanding/2015/lc/c5lc00614g (2023) (2015).

25. T. Guo, M., Rotem, A., A. Heyman, J. & A. Weitz, D. Droplet microfluidics for high-throughput biological assays. en. *Lab on a Chip* **12.** Publisher: Royal Society of Chem-

istry, 2146–2155. https://pubs.rsc.org/en/content/articlelanding/2012/lc/c2lc21147e (2023) (2012).

26. Unger, M. A., Chou, H.-P., Thorsen, T., Scherer, A. & Quake, S. R. Monolithic Microfabricated Valves and Pumps by Multilayer Soft Lithography. *Science* **288.** Publisher: American Association for the Advancement of Science, 113–116. https://www.science.org/doi/full/10.1126/science.288.5463.113 (2023) (Apr. 2000).

27. Cole, M. C., Desai, A. V. & Kenis, P. J. A. Two-layer multiplexed peristaltic pumps for high-density integrated microfluidics. en. *Sensors and Actuators B: Chemical* **151,** 384–393. ISSN: 0925-4005. https://www.sciencedirect.com/science/article/pii/S0925400510005873 (2023) (Jan. 2011).

28. Braun, E. The unforeseen challenge: from genotype-to-phenotype in cell populations. en. *Reports on Progress in Physics* **78.** Publisher: IOP Publishing, 036602. ISSN: 0034-4885. https://dx.doi.org/10.1088/0034-4885/78/3/036602 (2023) (Feb. 2015).

29. Acloque, H., Adams, M. S., Fishwick, K., Bronner-Fraser, M. & Nieto, M. A. Epithelial-mesenchymal transitions: the importance of changing cell state in development and disease. en. *The Journal of Clinical Investigation* **119.** Publisher: American Society for Clinical Investigation, 1438–1449. ISSN: 0021-9738. https://www.jci.org/articles/view/38019 (2023) (June 2009).

30. Trapnell, C. Defining cell types and states with single-cell genomics. en. *Genome Research* **25,** 1491–1498. ISSN: 1088-9051, 1549-5469. http://genome.cshlp.org/lookup/doi/10.1101/gr.190595.115 (2023) (Oct. 2015).

31. Simon, M. I., Strathmann, M. P. & Gautam, N. Diversity of G Proteins in Signal Transduction. en. *Science* **252,** 802–808. ISSN: 0036-8075, 1095-9203. https://www.science.org/doi/10.1126/science.1902986 (2023) (May 1991).

32. Tarazona, O. A. & Pourquié, O. Exploring the Influence of Cell Metabolism on Cell Fate through Protein Post-translational Modifications. en. *Developmental Cell* **54,** 282–292. ISSN: 1534-5807. https://www.sciencedirect.com/science/article/pii/S1534580720305438 (2023) (July 2020).

33. Cairns, R. A., Harris, I. S. & Mak, T. W. Regulation of cancer cell metabolism. en. *Nature Reviews Cancer* **11.** Number: 2 Publisher: Nature Publishing Group, 85–95. ISSN: 1474-1768. https://www.nature.com/articles/nrc2981 (2023) (Feb. 2011).

34. Zhao, S., Fung-Leung, W.-P., Bittner, A., Ngo, K. & Liu, X. Comparison of RNA-Seq and Microarray in Transcriptome Profiling of Activated T Cells. en. *PLOS ONE* **9.** Publisher: Public Library of Science, e78644. ISSN: 1932-6203. https://journals.plos.org/plosone/article?id=10.1371/journal.pone.0078644 (2023) (Jan. 2014).

35. Lowe, R., Shirley, N., Bleackley, M., Dolan, S. & Shafee, T. Transcriptomics technologies. en. *PLOS Computational Biology* **13.** Publisher: Public Library of Science, e1005457. ISSN: 1553-7358. https://journals.plos.org/ploscompbiol/article?id=10.1371/journal.pcbi.1005457 (2023) (May 2017).

36. Maier, T., Güell, M. & Serrano, L. Correlation of mRNA and protein in complex biological samples. en. *FEBS Letters. Systems Biology - Nobel Symposium 146* **583,** 3966–3973. ISSN: 0014-5793. https://www.sciencedirect.com/science/article/pii/S0014579309008126 (2023) (Dec. 2009).

37. Tang, F., Lao, K. & Surani, M. A. Development and applications of single-cell transcriptome analysis. en. *Nature Methods* **8.** Number: 4 Publisher: Nature Publishing Group, S6–S11. ISSN: 1548-7105. https://www.nature.com/articles/nmeth.1557 (2023) (Apr. 2011).

38. Zhang, W. *et al.* Comparison of RNA-seq and microarray-based models for clinical endpoint prediction. *Genome Biology* **16,** 133. ISSN: 1465-6906. https://doi.org/10.1186/s13059-015-0694-1 (2023) (June 2015).

39. Pan, Q., Shai, O., Lee, L. J., Frey, B. J. & Blencowe, B. J. Deep surveying of alternative splicing complexity in the human transcriptome by high-throughput sequencing. en. *Nature Genetics* **40.** Number: 12 Publisher: Nature Publishing Group, 1413–1415. ISSN: 1546-1718. https://www.nature.com/articles/ng.259 (2023) (Dec. 2008).

40. Wang, Z., Gerstein, M. & Snyder, M. RNA-Seq: a revolutionary tool for transcriptomics. en. *Nature Reviews Genetics* **10.** Number: 1 Publisher: Nature Publishing Group, 57–63. ISSN: 1471-0064. https://www.nature.com/articles/nrg2484 (2023) (Jan. 2009).

41. Altschuler, S. J. & Wu, L. F. Cellular Heterogeneity: Do Differences Make a Difference? en. *Cell* **141,** 559–563. ISSN: 0092-8674. https://www.sciencedirect.com/science/article/pii/S0092867410004873 (2023) (May 2010).

42. Brooks, M. D., Burness, M. L. & Wicha, M. S. Therapeutic Implications of Cellular Heterogeneity and Plasticity in Breast Cancer. en. *Cell Stem Cell* **17,** 260–271. ISSN: 1934-5909. https://www.sciencedirect.com/science/article/pii/S1934590915003690 (2023) (Sept. 2015).

43. Levitin, H. M., Yuan, J. & Sims, P. A. Single-Cell Transcriptomic Analysis of Tumor Heterogeneity. en. *Trends in Cancer. Special Issue: Physical Sciences in Oncology* **4,** 264–268. ISSN: 2405-8033. https://www.sciencedirect.com/science/article/pii/S2405803318300384 (2023) (Apr. 2018).

44. Jaitin, D. A. *et al.* Massively Parallel Single-Cell RNA-Seq for Marker-Free Decomposition of Tissues into Cell Types. *Science* **343.** Publisher: American Association for the Advancement of Science, 776–779. https://www.science.org/doi/full/10.1126/science.1247651 (2023) (Feb. 2014).

45. Goetz, J. J. & Trimarchi, J. M. Transcriptome sequencing of single cells with Smart-Seq. en. *Nature Biotechnology* **30.** Number: 8 Publisher: Nature Publishing Group, 763–765. ISSN: 1546-1696. https://www.nature.com/articles/nbt.2325 (2023) (Aug. 2012).

46. Picelli, S. *et al.* Full-length RNA-seq from single cells using Smart-seq2. en. *Nature Protocols* **9.** Number: 1 Publisher: Nature Publishing Group, 171–181. ISSN: 1750-2799. https://www.nature.com/articles/nprot.2014.006 (2023) (Jan. 2014).

47. Ramsköld, D. *et al.* Full-length mRNA-Seq from single-cell levels of RNA and individual circulating tumor cells. en. *Nature Biotechnology* **30.** Number: 8 Publisher: Nature Publishing Group, 777–782. ISSN: 1546-1696. https://www.nature.com/articles/nbt.2282 (2023) (Aug. 2012).

48. Macosko, E. Z. *et al.* Highly Parallel Genome-wide Expression Profiling of Individual Cells Using Nanoliter Droplets. en. *Cell* **161,** 1202–1214. ISSN: 0092-8674. https://www.sciencedirect.com/science/article/pii/S0092867415005498 (2023) (May 2015).

49. Zilionis, R. *et al.* Single-cell barcoding and sequencing using droplet microfluidics. en. *Nature Protocols* **12.** Number: 1 Publisher: Nature Publishing Group, 44–73. ISSN: 1750-2799. https://www.nature.com/articles/nprot.2016.154 (2023) (Jan. 2017).

CHAPTER 3

A VERSATILE DEEP LEARNING PLATFORM FOR TRACKING AND ANALYSIS OF ORGANOID DYNAMICS

3.1 Summary

Organoids have immense potential as ex vivo disease models for drug discovery and personalized drug screening. Dynamic changes in individual organoid morphology, number, and size can indicate important drug responses. However, these metrics are difficult and labor-intensive to obtain for high-throughput image datasets. Here, we present OrganoID, a robust image analysis platform that automatically recognizes, labels, and tracks single organoids, pixel-by-pixel, in brightfield and phase-contrast microscopy experiments. The platform was trained on images of pancreatic cancer organoids and validated on separate images of pancreatic, lung, colon, and adenoid cystic carcinoma organoids, which showed excellent agreement with manual measurements of organoid count (95%) and size (97%) without any parameter adjustments. Single-organoid tracking accuracy remained above 89% over a four-day time-lapse microscopy study. Automated single-organoid morphology analysis of a chemotherapy dose-response experiment identified strong dose effect sizes on organoid circularity, solidity, and eccentricity. OrganoID enables straightforward, detailed, and accurate image analysis to accelerate the use of organoids in high-throughput, data-intensive biomedical applications.

3.2 Project Background

Organoids are multicellular three-dimensional (3D) structures derived from primary or stem cells that are embedded into a biological matrix to create an extracellular environment that provides structural support and key growth factors. Organoids closely recapitulate cellular heterogeneity, structural morphology, and organ-specific functions of a variety of tissues,

which improves modeling of in situ biological phenomena compared to traditional monolayer cell cultures [1]. Live-cell imaging can reveal important features of organoid dynamics, such as growth, apoptosis/necrosis, movement, and drug responses, which can reflect physiological and pathological events such as organ development, function, infarction, cancer, and infection [2–7].

While organoids have been successfully used to investigate important phenomena that might be obscured in simpler models, their use in data-intensive applications, such as high-throughput screening, has been more difficult. A major challenge for organoid experiments is drug-response measurement and analysis, which must be performed for a large number of microscopy images. Image analysis is particularly difficult for organoid experiments due to the movement of organoids across focal planes and variability in organoid size and shape between different tissue types, within the same tissue type, and within the same single culture sample [8, 9]. Several recently developed organoid platforms, while powerful, rely on per-experiment or per-image tuning of brightfield image analysis parameters [10–12], or require manual labeling of each image [7, 13, 14], which limits experiment reproducibility and scale. Organoids can be fluorescently labeled to aid in image segmentation and tracking, such as through genetic modification for fluorescent protein expression [15–17], cell fixation and staining [10, 16], or the use of membrane-permeable dyes. However, these approaches may alter intrinsic cellular dynamics from original samples [18, 19], limit measurements to endpoint assays, or cause cumulative toxicity through longer growth times and limited diffusion through the hydrogel matrix [20]. There is a critical need for an automated image analysis tool that can robustly and reproducibly measure live-cell organoid responses in high-throughput experiments without the use of potentially toxic or confounding fluorescence techniques.

A number of software tools have been developed to automate the process of brightfield and phase-contrast organoid image analysis. These platforms use conventional image processing

methods, such as adaptive thresholding and mathematical morphology [21], or convolutional neural networks [22–24] to identify organoids in sequences of microscopy images. Despite their advantages, many existing platforms require cellular nuclei to be transgenically labeled [23], which increases experiment time and complexity and may modify cellular dynamics. Other existing platforms require manual tuning of parameters for each image [21], focus on single-timepoint analysis [24], only provide population-averaged (bulk) measurements without single-organoid resolution, or are limited to bounding-box detection [22], which fails to capture potentially useful morphological information at the individual organoid level. Changes in organoid shape, such as spiking or blebbing, can reveal important responses to external stimuli and might be missed with bounding-box measurements [25]. Many of these existing platforms were also developed for the analysis of organoids derived from a single type of tissue and for images obtained with one specific optical configuration, precluding their use across different experimental settings.

To address these challenges, we have developed a software platform, OrganoID, that can identify and track individual organoids in a population derived from a wide range of tissue types, pixel by pixel, in both brightfield and phase-contrast microscopy images and in time-lapse experiments. OrganoID consists of (i) a convolutional neural network, which detects organoids in microscopy images, (ii) an identification module, which resolves contours to label individual organoids, and (iii) a tracking module, which follows identified organoids in time-lapse imaging experiments. Most importantly, OrganoID was able to accurately segment and track a wide range of organoid types, including those derived from pancreatic ductal adenocarcinoma, adenoid cystic carcinoma, and lung and colon epithelia, without cell labeling or parameter tuning. The OrganoID software overcomes a major hurdle to organoid image analysis and supports wider integration of the organoid model into high-throughput applications.

3.3 Design and Implementation

3.3.1 A convolutional neural network for pixel-by-pixel organoid detection

We developed a deep learning-based image analysis pipeline, OrganoID, that recognizes and tracks individual organoids, pixel by pixel, for bulk and single-organoid analysis in brightfield and phase-contrast microscopy images (Figure 3.1a). The platform employs a convolutional neural network to transform microscopy images into organoid probability images, where brightness values represent the network belief that an organoid is present at a given pixel. The network structure was derived from the widely successful u-net approach to image segmentation [26] (Figure 3.1b). The u-net approach first passes each image through a contracting series of multidimensional convolutions and maximum filters to extract a set of deep feature maps that describe the image at various levels of detail and contexts, such as edges, shapes, and textures. The feature maps are then passed through an expanding series of transposed convolutions, which learn to localize the features and assemble a final output.

The OrganoID neural network follows the u-net structure and was optimized to require far fewer feature channels than the original implementation, as a reduction in trainable model parameters limits overfitting and minimizes the amount of memory and computational power required to use the network in the final distribution [27]. The original u-net implementation uses 64 filters in the first layer, which results in quite a large number of trainable parameters across the full network (over 30 million) [26]. We sequentially reduced the number of filters in the first layer by powers of two to reach a minimal value that preserved performance on the validation dataset (validation mean IOU was 0.088 for 8 filters in the first layer, compared to 0.098 for 4 filters and 0.1 for 16 filters). The final OrganoID u-net structure uses only 8 filters in the first layer, which results in a network structure with less than 500,000 trainable parameters (a 98% reduction compared to the original implementation). All convolutional

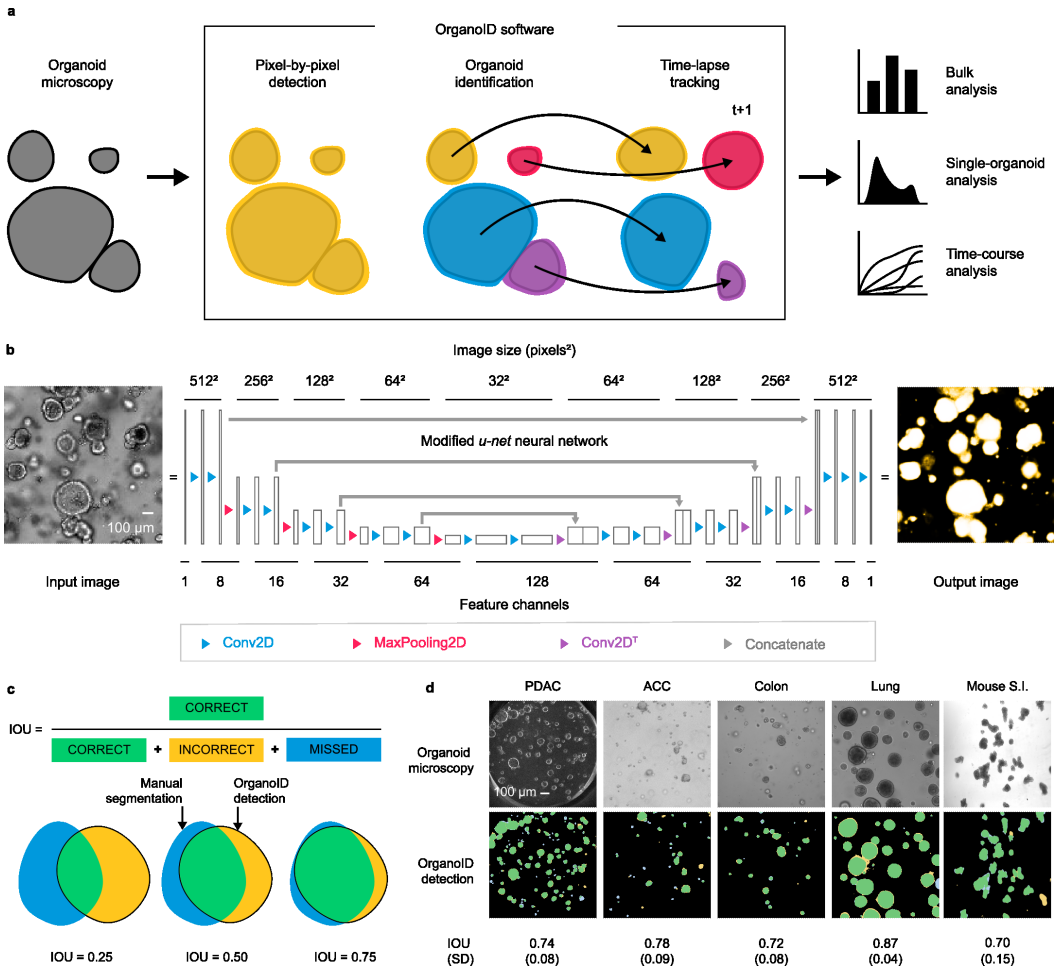

Figure 3.1: Architecture and evaluation of the OrganoID platform and neural network. (a) The OrganoID software automates robust analysis of organoid microscopy images. Contours are detected pixel by pixel and then separated into distinct organoids for bulk or single-organoid analysis. Identified organoids can also be tracked across time-lapse image sequences to follow responses over time. (b) Microscopy images are processed by a convolutional neural network to produce images that represent the probability that an organoid is present at each pixel. The network follows the u-net architecture, which applies a series of two-dimension convolutions, maximum filters, and image concatenations to extract and localize image features. Feature channel depths were minimized to limit overfitting and computational power required to use the tool. Scale bar 100 µm. (c) The intersection-over-union (IOU) metric, defined as the ratio of the number true positive pixels to the union of all positive pixels, was used to measure the quality of the neural network detections. To compute the IOU, pixels above 0.5 in the network prediction image were marked as positives. Examples of IOU values for several degrees of overlap are shown. (d) A representative set of images of different organoid types from the test dataset are shown with the corresponding OrganoID detections. Detections are overlayed on top of ground truth measurements and colored according to the schema in (c). The mean and standard deviation of IOU for images of each organoid type in the test dataset are also shown. Scale bar 100 µm.

neurons were set to compute outputs with the exponential linear unit activation function, which has been previously shown to produce higher accuracy than the rectified linear unit (ReLU, used in the original u-net implementation) and avoid vanishing gradient problems during network training [28]. Neurons in the final convolutional layer were set with a sigmoid activation function to produce a normalized output that corresponds to the probability that an organoid is present at each pixel in the original image. All images are automatically contrasted and resized to 512x512 pixels before training and inference. Python was used for the entire OrganoID platform and Keras (a neural network interface for the TensorFlow software library) was used for network expression, training, and operation.

An original dataset of 66 brightfield and phase-contrast microscopy images of organoids were manually segmented to produce black-and-white ground truth images for network training (52 image pairs) and validation (14 image pairs) (S1a Fig). Each image featured 5 to 50 organoids derived from human pancreatic ductal adenocarcinoma (PDAC) samples from two different patients. Organoids were either grown on a standard tissue culture plate or on a microfluidic organoid platform [29]. To teach the network that segmentations should be independent of imaging orientation, field of view, lens distortion, and other potential sources of overfitting, the training dataset was processed with the Augmentor Python package [30] with random rotation, zoom, elastic distortion, and shear transformations to produce an augmented set of 2,000 images for training (S1b Fig). The neural network was trained on this dataset with the Adam stochastic optimization algorithm [31] at a learning rate of 0.001. Unweighted binary cross-entropy between predicted and ground-truth segmentations was used for the loss function. Layer weights were initialized with the He method [32]. An early stopping rule was used to halt training once performance on the validation dataset reached a minimum (i.e. once 10 epochs pass with no improvement in validation loss). The batch size was set to train on 8 augmented images for every round of backpropagation. Dropout regularization was introduced after all convolutions to randomly set 12.5% of neuron weights

to zero after each batch. After each epoch, a copy of the model was saved for additional evaluation of the training process

3.3.2 Identification of individual organoids with diverse morphology and size

The convolutional neural network detects organoids in an image on a pixel-by-pixel basis, which can be used to measure bulk responses. For single-organoid analysis, pixels must be grouped together to identify individual organoids. This task is straightforward for isolated organoids, where all high-belief pixels in a cluster correspond to one organoid, but is more difficult for organoids that are in physical contact. To address this challenge, we developed an organoid separation pipeline (Fig 2a) that uses the raw network prediction image to group pixels into single-organoid clusters. Conventionally, neural network image segmentation methods set an absolute threshold on predicted pixels to produce a binary detection mask. This approach is effective but discards useful information about the strength of predictions. The segmentations that were used to train the neural network were produced with a 2-pixel boundary between organoids in contact that follows the contour of separation. As a result, the network predictions were marginally less confident about pixels near organoid boundaries (Fig 2a). We took advantage of this phenomenon to identify organoid contours with a Canny edge detector [33], an image transformation which (i) computes the partial derivative of pixel intensity to identify high-contrast areas, (ii) blurs the image to smooth noisy regions, and (iii) applies a hysteresis-based threshold to identify locally strong edges. Edges are removed from the thresholded prediction image to mark the centers of each organoid. These centers are then used as initializer basins in a watershed transformation [34], an algorithm inspired by the filling of geological drainage basins that is used to segment contacting objects in an image. The image is further refined to remove organoids that may be partially out of the field-of-view or below a particular size threshold. The pipeline outputs a labeled image, where the pixels that represent an individual organoid are all set to a unique organoid ID

number, which can be used for single-organoid analysis (Fig 2a).

The scipy [35] and scikit-image [36] packages were used to identify individual organoids from the network detection images. Detection images were thresholded at 0.5 and passed through a morphological opening operation to remove weak and noisy predictions. Partial derivatives were computed with a Sobel filter, passed through a Gaussian filter ($\sigma = 2$), and converted to an edge mask with a hysteresis threshold filter ($T_{hi} = 0.05$, $T_{lo} = 0.005$), which was then was used to mark organoid centers. The watershed method was used to identify filled organoid contours, with the organoid centers as label initializers and the network prediction image as an inverted heightmap. Labeled organoids were morphologically filled and discarded if the total area was below 200 pixels. Images were morphologically processed with scikit-image to record properties of identified organoids.

3.3.3 Automated organoid tracking in time-lapse microscopy experiments

OrganoID was also developed with a tracking module for longitudinal single-organoid analysis of time-course imaging experiments, where changes in various properties of individual organoids, such as size and shape, can be measured and followed over time. The central challenge for the tracking module is to match a detected organoid in a given image to the same organoid in a later image. The OrganoID tracking algorithm builds a cost-assignment matrix for each image in a time-lapse sequence, where each row corresponds to an organoid tracked from a previous image and each column corresponds to an organoid detected in the current image. Each matrix entry is the cost of assigning a given organoid detection in the current image to a detection in the previous image. The cost function was defined as the inverse of the number of shared pixels between the two organoids. As such, the assignment cost between two detections will be minimal for those that are of similar shape and in a similar location. The cost-assignment matrix is also padded with additional rows and columns to allow for "pseudo-assignments" that represent missing or newly detected organoids. Finally, the

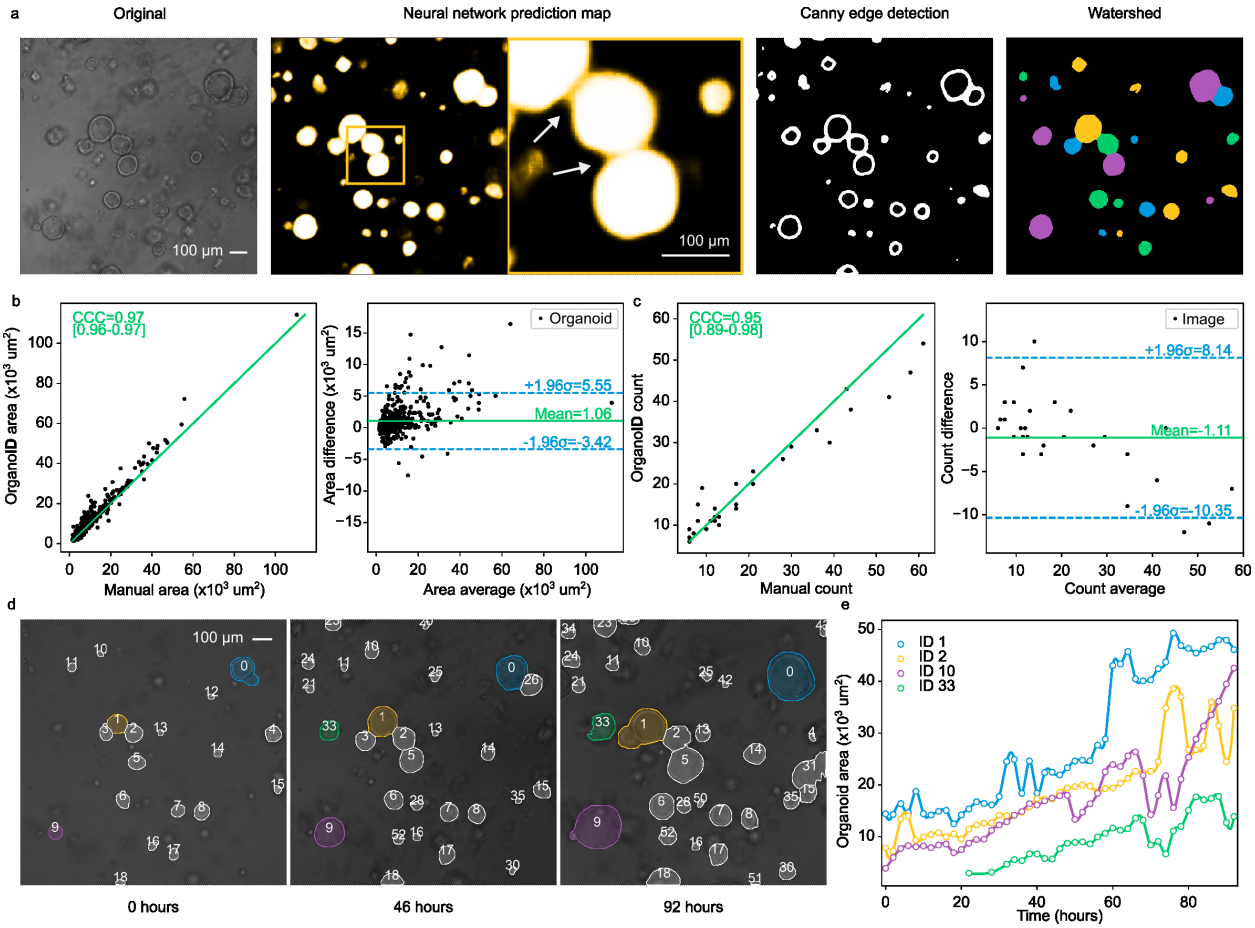

Figure 3.2: OrganoID can identify individual organoid contours, including those in physical contact. (a) An example image (left) is shown to demonstrate the steps of single-organoid identification. The neural network predictions (second-from-left) are observably less confident for pixels at organoid boundaries (enlarged view, indicated with white arrows), which enables edge detection with a Canny filter (second-from-right). Edges are used to identify organoid centers, which serve as basin initializers for a watershed transformation on the prediction image to produce a final single-organoid labeled image (right). (b) The identification pipeline was used to count the number of organoids in images from the test dataset. These counts were compared to the number of organoids in the corresponding manually segmented images. The concordance correlation coefficient (CCC) was computed to quantify measurement agreement (left). Bland-Altman analysis (right) demonstrates low measurement bias and limits of agreement. Black dots are test images. Green line in the left plot is y=x. (c) The area of each organoid in all test images was also measured manually and with OrganoID. Measurements were compared with CCC computation (left) and Bland-Altman analysis (right). Black dots are identified organoids. (d) Identified organoids in time-lapse microscopy images are matched across frames to generate single-organoid tracks and follow responses over time. Shown are images of three timepoints from an organoid culture experiment. (e) Automatically measured growth curves for a selected set of organoids from the experiment in (d).

Munkres variant of the Hungarian algorithm [37] was used to minimize the cost-assignment matrix to find an optimal matching between organoid detections in the previous image and the detections in the current image. This approach produces organoid "tracks" for unique organoids in time-lapse images.

3.4 Results

Network training halted after 37 epochs, when segmentation error (binary cross-entropy) on the validation dataset converged to a minimal value (S1c Fig and S1 Video). After hyperparameter tuning, the final model performance was assessed on a novel PDAC organoid testing dataset, previously unseen by the network. Performance was quantified with the intersection-over-union (IOU) metric, which is defined as the overlap between the predicted and actual organoid pixels divided by their union (Fig 1c). An IOU greater than 0.5 is generally considered to reflect a good prediction [38,39] and we chose this value to be the minimal benchmark for satisfactory model performance. All PDAC images passed the benchmark, with a mean IOU of 0.74 (SD = 0.081) (S2 Fig).

Because the network was trained and assessed solely with images of PDAC organoids, we were also curious to evaluate its capacity to generalize to organoids derived from non-PDAC tissues. Microscopy images of organoids derived from lung epithelia, colon epithelia, and salivary adenoid cystic carcinoma (ACC) were manually segmented (6 images for each tissue type). The OrganoID network passed the benchmark for all of these non-PDAC images, with a mean IOU of 0.79 (SD=0.096) (S2 Fig). Additionally, 19 images of organoids derived from mouse small intestine were segmented and evaluated with the model and passed the benchmark with a mean IOU of 0.70 (SD=0.15). These results support the potential of the OrganoID neural network to generalize to organoids from various tissues of origin without parameter tuning (Fig 1d). However, 3 images of mouse small intestinal organoids did not pass the benchmark, which suggests a limit to this generalizability. To demonstrate

how performance can be improved on novel datasets, a copy of the neural network was additionally trained on a subset of mouse small intestinal organoid images. This retrained network showed considerable improvement on a test dataset of mouse intestinal organoids with a mean IOU of 0.82 (SD=0.09) while maintaining performance on the original test dataset with a mean IOU of 0.76 (SD=0.10) (S2 Fig).

The network was also evaluated for appropriate exclusion of non-organoid technical artifacts. Air bubbles in culture media or gel matrix were rarely detected by OrganoID with a false positive rate of 4.2% (S3a Fig). We observed that OrganoID segmentations also avoided cellular debris or dust embedded into the gel, ignored chamber borders, and performed robustly across microscope resolutions, organoid concentrations, and organoid shapes (S3b-g Fig). OrganoID proved to be computationally efficient; each image was segmented in 300 milliseconds on a laptop CPU (Intel i7-9750H, 2.6GHz) with less than 200 megabytes of RAM usage.

For quantitative validation of single-organoid analysis, OrganoID was used to count and measure the area of organoids in images from the PDAC and non-PDAC human testing datasets (a total of 28 images). These data were then compared to the number and area of organoids in the corresponding manually segmented images. Organoid counts agreed with a concordance correlation coefficient (CCC) of 0.95 [95% CI 0.89-0.98]. OrganoID, on average, detected 1.1 fewer organoids per image than manual segmentation. The limits of agreement between OrganoID and manual counts were between -10.35 and 8.14 organoids (Fig 2b). Organoid area comparison demonstrated a CCC of 0.97 [95% CI 0.96-0.97]. OrganoID area measurements were biased to be $1.06 * 10^3 \mu m^2$ larger per organoid with limits of agreement between $-3.42 * 10^3 \mu m^2$ and $5.55 * 10^3 \mu m^2$ (Fig 2c). Several additional morphological metrics were calculated, including circularity (the ratio of the organoid perimeter to the perimeter of a perfect circle), eccentricity (a measure of elliptical deviation from a circle), and solidity (the ratio of the organoid area to the area of its convex hull). These three metrics showed

moderate concordance (0.52, 0.41, and 0.59 respectively) between automated and manual measurements (S4 Fig). Performance on brightfield microscopy images was higher than performance on phase-contrast microscopy images. Overall, the measurements produced by OrganoID were in considerable agreement with those obtained by hand in our test dataset, which supports the use of OrganoID for automated single-organoid analysis.

For validation of the organoid tracking module, microscopy images taken every 2 hours from a 92-hour organoid culture experiment were passed through the entire OrganoID pipeline to produce growth curves that followed single-organoid changes over time (Fig 2d-e). The tracking step was also performed by hand to evaluate automated performance. OrganoID tracking maintained over 89% accuracy (defined as the fraction of identified organoids that were correctly matched at each time step) throughout the duration of the experiment (S5 Fig and S2 Video). Tracking accuracy was not affected when frames were discarded to simulate a 12-hour imaging interval, which demonstrates low susceptibility to imaging frequency.

3.4.1 OrganoID normalizes single-organoid death responses over time

PDAC organoids were treated with serial dilutions of gemcitabine (3nM-1000nM), an FDA-approved chemotherapeutic agent commonly used to treat pancreatic cancer. Propidium iodide (PI), a fluorescent reporter of cellular necrosis, was also added to the culture media to monitor death responses. Cultures were then imaged every 4 hours over 72 hours and the produced brightfield images were processed with the OrganoID platform to identify organoids and analyze timelapse features (Fig 3a). At gemcitabine concentrations above 3 nM, the total organoid area increased for the first several hours, which reflected initial organoid growth, but then decreased to a value and at a rate inversely proportional to gemcitabine concentration (Fig 3b). Identified organoid counts for gemcitabine concentrations above 10 nM also sharply decreased over time. The total fluorescence intensity of the PI signal increased over time to

a value and at a rate proportional to gemcitabine concentration, however the response to 100 nM gemcitabine appeared to induce a stronger death signal than the response to 1000 nM gemcitabine (Fig 3c).

Measurements of death stains such as PI are typically normalized to a viability measurement that accounts for differences in the number and size of organoids between replicates that can compound over the duration of an experiment. We hypothesized that OrganoID could be used to measure morphological features indicative of organoid viability over time, which could then be used to normalize and decrease the variability of measurements across experimental replicates. Furthermore, organoid tracking with OrganoID would enable per-organoid measurement normalization, which we observed to significantly decrease the coefficient of variation of organoid area and fluorescence change across organoids imaged at the same time point and exposed to the same concentration of gemcitabine (S6 Fig). Normalization of PI intensity with tracked single-organoid area indeed increased the separation of responses between each treatment group over time, decreased standard error across replicates, and corrected the response discrepancy between the 100 nM and 1000 nM conditions (Fig 3c). We also compared dose-response measurements to an MTS proliferation assay ((3-(4,5-dimethylthiazol-2-yl)-5-(3-carboxymethoxyphenyl)-2-(4-sulfophenyl)-2H-tetrazolium), a gold-standard indicator of cell viability, at the experiment endpoint. The MTS assay determined the half-maximal effective concentration (EC50) to be 26.13 nM of gemcitabine. However, total fluorescence and organoid area underestimated this value to be 16.95 nM and 12.67 nM, respectively. In contrast, the dose response of area-normalized fluorescence determined the EC50 to be 24.45 nM, considerably closer to the MTS standard (Fig 3d).

3.4.2 OrganoID uncovers morphology changes predictive of drug response

Changes in organoid morphology can indicate important phenotypic responses and state transitions. For example, some tumor organoid models grow into structures with invasive

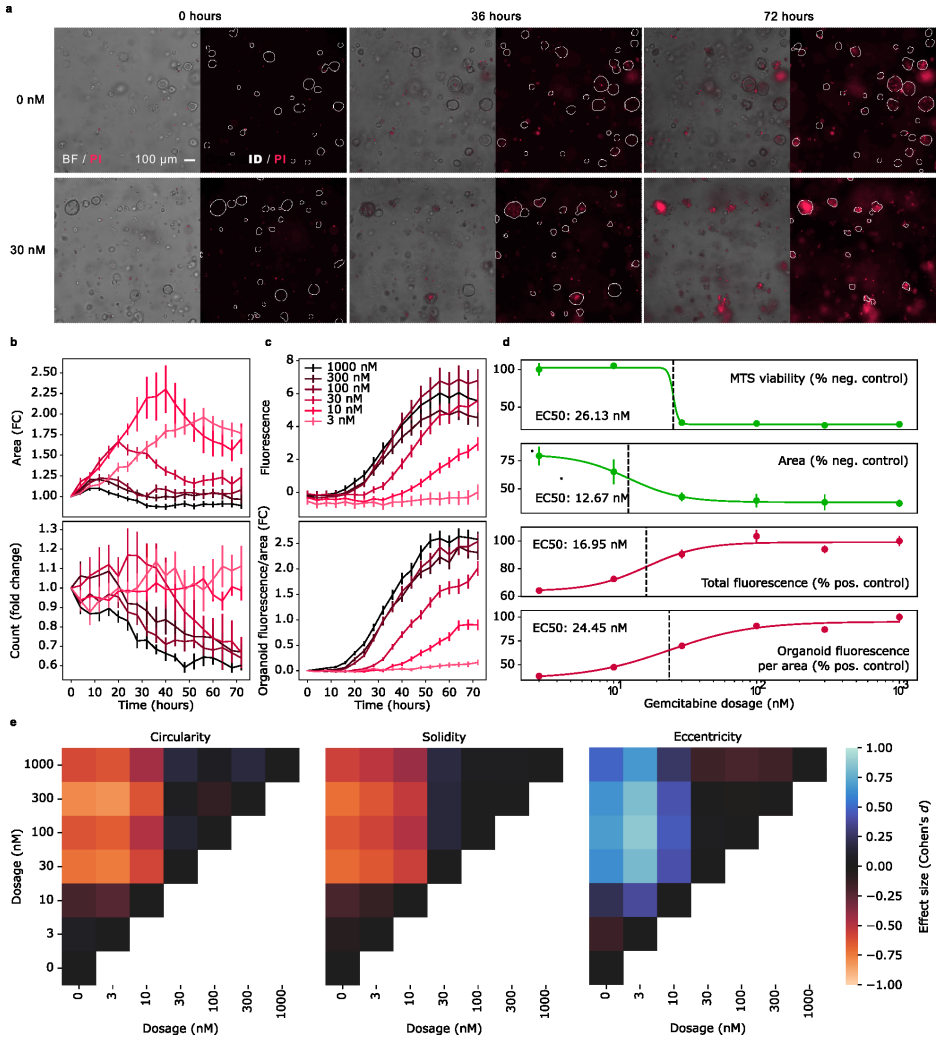

Figure 3.3: OrganoID facilitates morphological analysis of a chemotherapeutic dose-response experiment. (a) PDAC organoids were treated with gemcitabine. Propidium iodide (PI) was used to label dead organoids. Shown are representative images from three time points for control and 30 nM gemcitabine. OrganoID identified organoid contours, displayed on top of the PI channel. (b) OrganoID measurements of fold change (FC) area (top) and number of organoids (bottom) over time for each concentration of gemcitabine. Error bars represent standard error of the mean (n=6). (c) Total PI intensity for each concentration of gemcitabine (top). Fluorescence intensity per area of each organoid were normalized to first detection, which reduced standard error across replicates (bottom). (d) Organoid area, total fluorescence, and area-normalized fluorescence were used to estimate the half-maximal effective concentration (EC50) without live-cell staining, and compared to an MTS viability assay. (e) Circularity (area divided by area of a perfect circle with equivalent perimeter), solidity (area divided by area of the convex hull), and eccentricity (elliptical deviation from a perfect circle), were computed for each organoid. Effect sizes (Cohen's d statistic) between each gemcitabine concentration are shown, computed from dosages on the x-axis to dosages on the y-axis.

projections into the culture matrix, reflecting epithelial-mesenchymal transition; the addition of certain chemotherapeutic agents prevents development of these protrusions with minimal effects on overall organoid size [25]. These important responses can be investigated through single-organoid image analysis that captures the precise contour of each organoid. We used OrganoID to automatically profile the morphology of individual organoids across the gemcitabine dose-response experiment. Organoid circularity, solidity, and eccentricity showed sigmoidal dose responses and determined the endpoint EC50 to be 28.47 nM, 27.05 nM, and 18.08 nM, respectively (S7 Fig). The effect size of gemcitabine concentration on these shape metrics was also computed with Cohen's d statistic, defined as the ratio of the difference in means to the pooled standard deviation. Gemcitabine dosage had a moderate to large endpoint effect on organoid circularity, solidity, and eccentricity across concentrations below and above the EC50 (Fig 3e). Circularity and solidity decreased at higher concentrations, while eccentricity increased, reflecting disrupted organoid morphology. This worked example demonstrates the advantages of OrganoID for automated bulk and single-organoid morphological analysis of time-course experiments without the need for live-cell fluorescence techniques.

3.5 Discussion and Future Directions

Organoids have revolutionized biomedical research through improved model representation of native tissues and organ systems. However, the field has yet to fully enter the high-throughput experimental space. A central bottleneck is the challenge of automated response measurement and analysis in large numbers of microscopy images. Organoids exhibit striking diversity in morphology and size and can move through their 3D environment into and out of the focal plane; current image processing tools have not quite been able to capture these aspects in a robust manner. We developed OrganoID to bridge this gap and automate the process of accurate pixel-by-pixel organoid identification and tracking over space and time.

Experimental replicates in organoid studies can differ in the number and distribution of sizes of organoids. This difference between identical conditions requires per-sample normalization of response measurements to baseline growth of organoid colonies. There are several commercially available live-cell assays that can facilitate normalization in 2D culture. However, these same assays have proven difficult for organoid use due to the production of toxic photobleaching byproducts, limited diffusion through the gel matrix, and nonspecific staining of the gel matrix that results in a considerable background signal. Another available option is to genetically modify each organoid sample to express fluorescent proteins; however, this method increases experimental time and complexity and may alter cellular dynamics from the original tissue sample. The OrganoID platform can be leveraged for accurate normalization of standard organoid assays without live-cell fluorescence methods. OrganoID is also uniquely useful for efficient quantification of single-organoid morphological features, such as circularity, solidity, and eccentricity, that can reflect important dynamic responses. In our gemcitabine dose-response experiment, we observed that PDAC organoid circularity and solidity decreased with an increase in gemcitabine dosage. This disturbance of organoid architecture is likely due to the interference of gemcitabine with RNA and DNA synthesis[40], which may in turn affect cell turnover and production of signaling and structural proteins.

In this work, we have also contributed a manually segmented organoid image dataset for use in other computational platforms. OrganoID has demonstrated compatibility with organoids of various sizes, shapes, and sample concentrations as well as various optical configurations. Most excitingly, the OrganoID model was trained and validated on images of PDAC organoids but still demonstrated excellent generalization to images of other types of organoids, including those derived from colon tissue, lung tissue, and adenoid cystic carcinoma.

OrganoID was trained with and tested on a diverse yet relatively small set of images. Despite the suggested generalizability of OrganoID to various samples and optical configu-

rations, performance may still differ for untested organoids types. Performance on a dataset of mouse small intestinal organoids passed our benchmark on average, however there were several challenging images that were not processed adequately. We demonstrated further training on a handful of images of mouse small intestinal organoids to improve performance on such challenging datasets. As well, OrganoID can only detect and assign a single organoid to each pixel in an image. While the platform can appropriately identify contours of organoids in physical contact, it cannot distinguish organoids that overlap across the focal plane. These limitations could be overcome in future work with a network model that produces multiple outputs per pixel as well as additional validation, an expanded training dataset, and the use of multiple focal planes for image analysis.

We have released the OrganoID platform open-source and freely licensed on GitHub (https://github.com/jono-m/OrganoID). The repository includes all source code as well as usage instructions and scripts used for the examples presented in this paper. The network training module is also included on the repository to improve performance for any untested applications. The image dataset is available at through the Open Science Framework (https://osf.io/xmes4/). Our image analysis platform serves as an important tool for the use of organoids as physiologically relevant models in high-throughput research. The platform can accurately capture detailed morphological measurements of individual organoids in live-cell microscopy experiments without the use of genetic modifications or potentially cytotoxic dyes. These metrics can reveal important organoid responses that might be missed with the use of bounding-box tools. The ability of the platform to generalize to a range of organoid types without parameter tuning reflects the potential for the platform to standardize morphological assay readouts and improve measurement reproducibility. OrganoID achieves comprehensive and expedient image analysis of organoid experiments to enable broader use of organoids as tissue models for high-throughput investigations into biological systems.

3.6 Supporting Information

3.6.1 Supplementary Figures

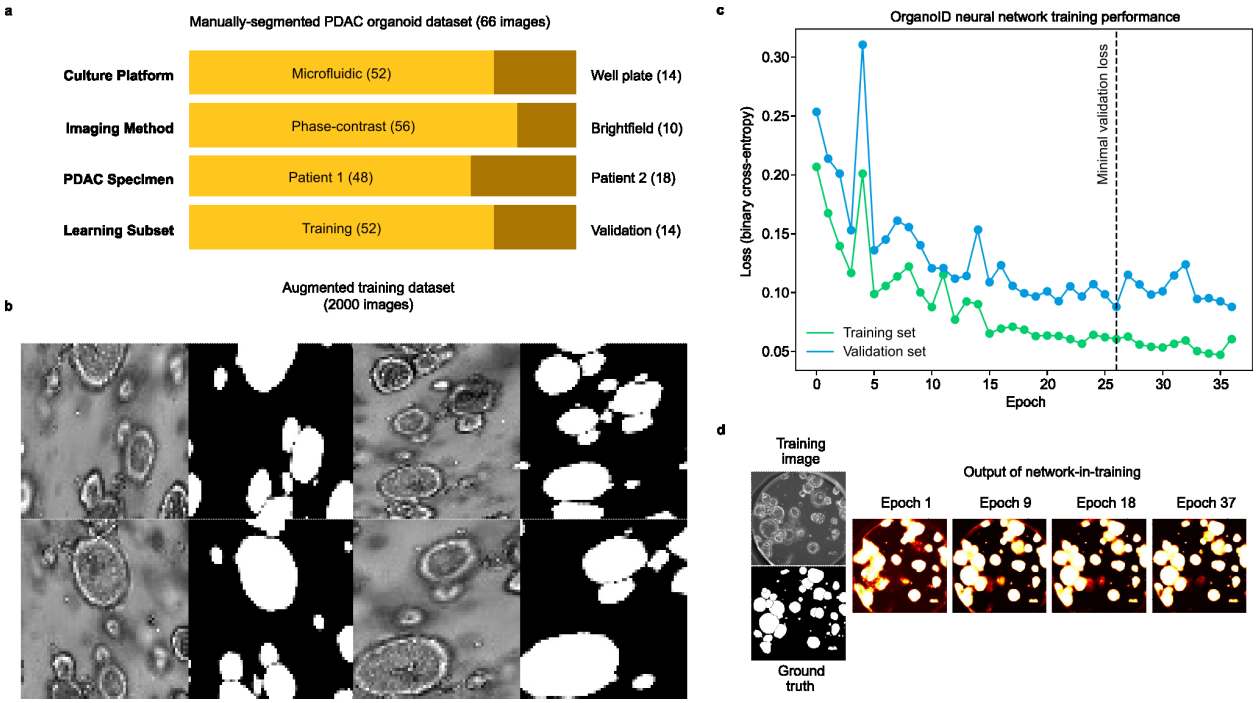

Figure 3.4: Network training performance. (a) The network was trained on 66 manually labeled microscopy images of organoids derived from pancreatic ductal adenocarcinoma (PDAC) samples from two patients. Organoids were cultured in a well plate or microfluidic format and imaged through phase-contrast or brightfield microscopy. Images were then split into datasets for network training (80%) and validation (20%). (b) The 52 images in the training dataset were passed through a series of random transformations to produce an augmented dataset of 2,000 images. (c) Network training was stopped after 37 epochs, once a minimum binary cross-entropy loss on the validation dataset was reached. (d) The OrganoID neural network predicts the probability that an organoid is present at each pixel. Shown are network predictions produced by intermediate models at selected epochs through the training process.

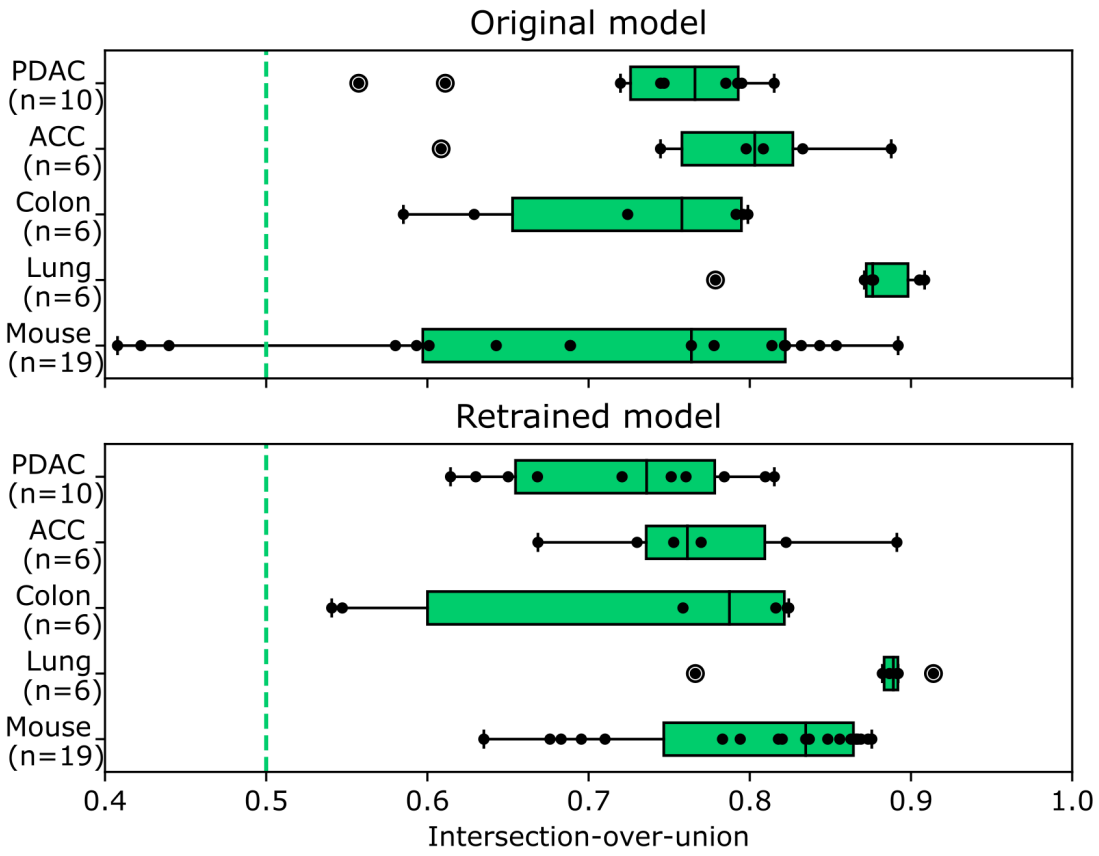

Figure 3.5: Network test dataset performance. A test set of images of organoids derived from human PDAC, salivary adenoid cystic carcinoma (ACC), colon epithelia, distal lung epithelia, and mouse small intestine were manually segmented to assess network performance (top). An IOU of 0.5 was set as a benchmark for a successful network prediction (dashed green line). All images of human organoids in the test set passed the benchmark, which demonstrates the capacity of the PDAC-trained network to generalize to other organoid types. Several of the mouse organoids did not pass the benchmark, and so the model was later retrained with part of this dataset included to demonstrate extensibility (bottom).

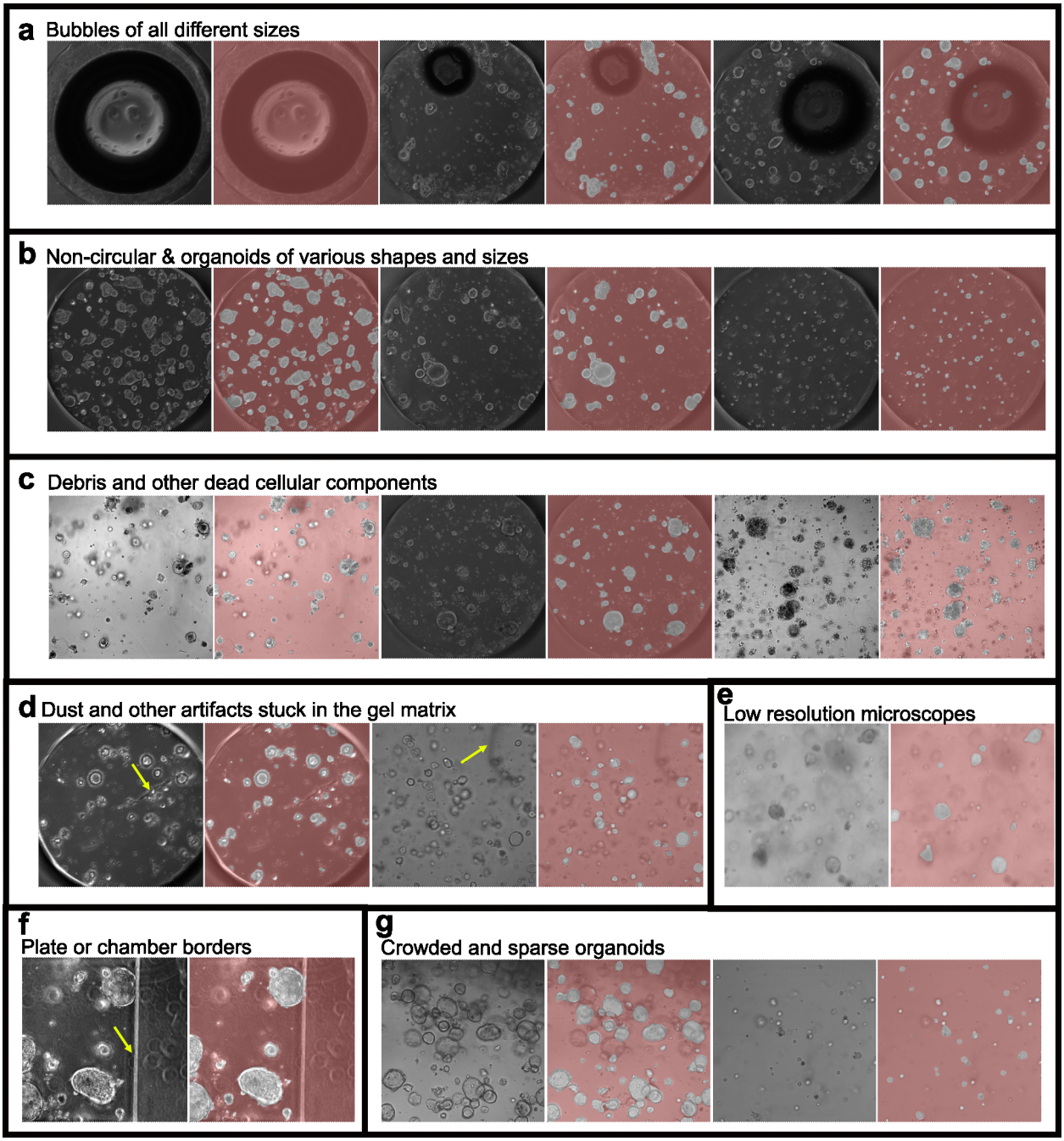

Figure 3.6: Exclusion of non-organoid artifacts. OrganoID ignored bubbles (a), debris (c-d), and plate or microfluidic chamber borders (f) to accurately identify organoids that exhibit diverse morphology and sizes, even within a single sample (b). OrganoID can also handle various optical configurations, including low-resolution or poorly-lit images (e). Gel droplets can support densely-packed or isolated organoids, which can all be detected with OrganoID (g).

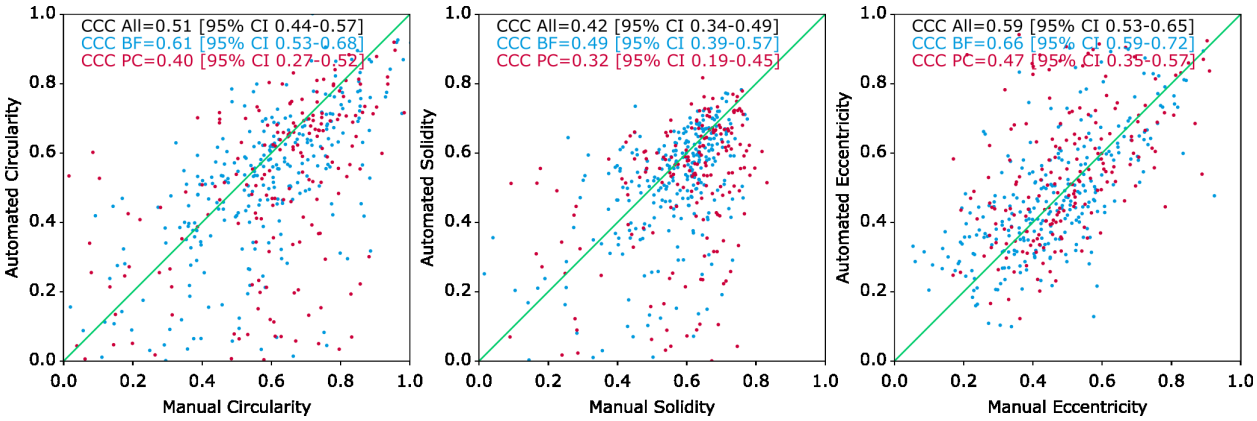

Figure 3.7: Evaluation of organoid shape measurement. OrganoID was used to measure organoid circularity (ratio of organoid area to the area of a perfect circle with equal perimeter), solidity (ratio of organoid area to area of the convex hull), and eccentricity (elliptical deviation from a circle). These measurements were then compared to those from manual segmentation. The concordance correlation coefficient (CCC) was computed for all organoids, as well as for organoids imaged through phase contrast (PC, red) or brightfield (BF, blue) microscopy. For calculation of CCC for circularity and solidity (bounded to 0-1, with most values near 1), the data was first logit-transformed.

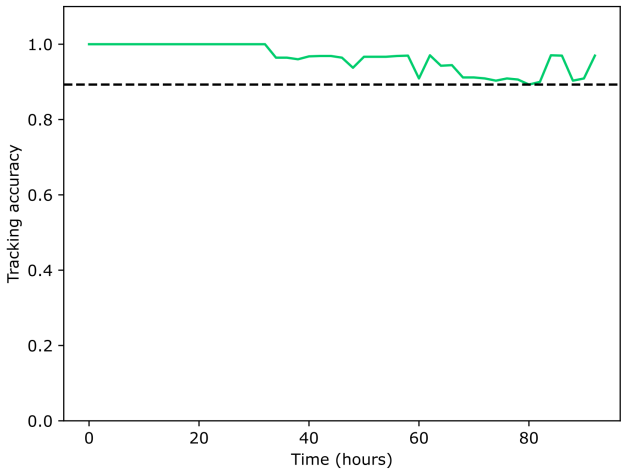

Figure 3.8: Tracking accuracy over time. A time-lapse microscopy experiment was analyzed with OrganoID to identify organoids in each image. OrganoID was then used to match identified organoids across frames to build single-organoid tracks. The identified organoids were also matched by hand to assess tracking performance. Accuracy was defined the number of organoid track labels in agreement divided by the total number of organoids present at each frame.

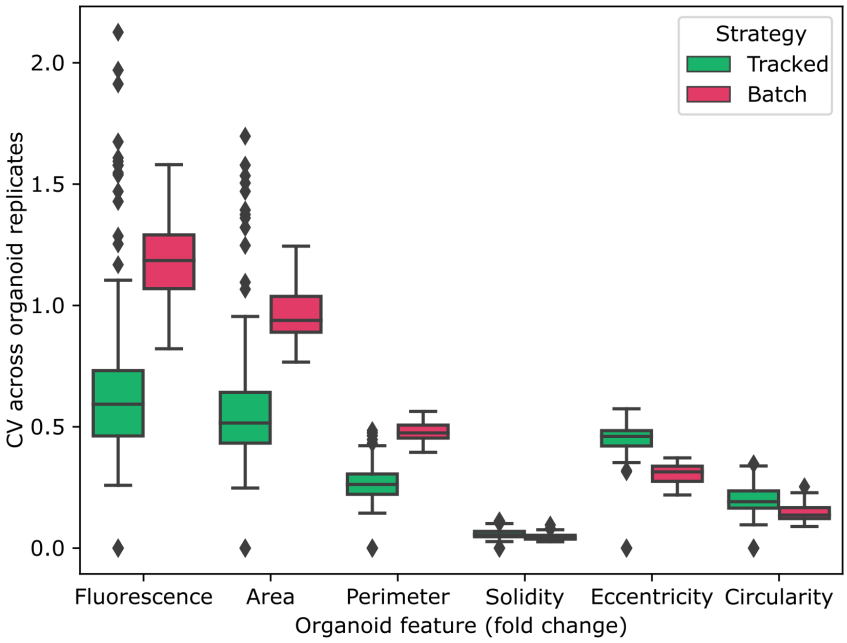

Figure 3.9: Comparison of batch vs. tracked normalization. In batch analysis, measurements of organoids exposed to the same gemcitabine dosage for the same duration were normalized to the average of organoids at t=0. In tracked analysis, organoid measurements are instead normalized to each individual organoid measurement when initially detected by the tracking algorithm. The coefficient of variation (CV) was significantly lower with tracked analysis for change in fluorescence (Welch's t-test p=2e-30), area (p=2e-29) and perimeter (2e-63). CV was significantly higher with tracked analysis for eccentricity (p=7e-25) and circularity (p=2e-12).

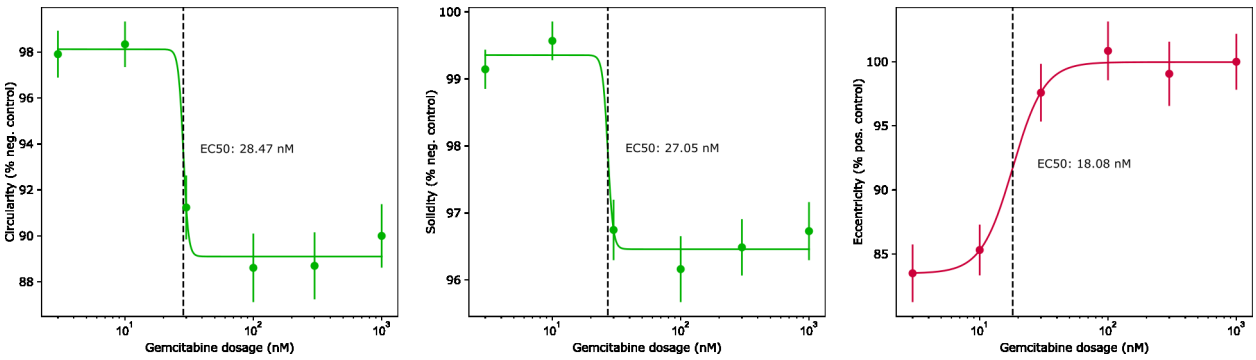

Figure 3.10: Dose response of shape metrics. Organoid circularity, solidity, and eccentricity were observed to follow sigmoidal dose responses to gemcitabine.

3.6.2 Supplementary Methods

Organoid culture and image acquisition

Tumor organoid cultures derived from pancreatic adenocarcinoma (PDAC) patients were isolated and prepared as previously described [29]. PDAC organoids were cultured and imaged in a microfluidic platform [30] or a 24-well suspension culture plate (Thermo Fisher, 144530). Human colonic organoids were cultured similarly to PDAC organoids, with Matrigel and growth or differentiation media as described in established methods [29]. Distal respiratory organoids were obtained from the Ishay-Ronen Lab at the Sheba Medical Center and cultured through a previously described protocol [31] in 24-well plates. Images of adenoid cystic carcinoma (ACC) organoids and mouse small intestinal organoids were obtained from Dr. Weber and colleagues from University of Chicago Medicine. The pancreatic and airway lung organoids were cultured and imaged on an automated translational stage of an inverted microscope (Nikon Eclipse Ti) enclosed in an environmentally controlled chamber (Life Imaging Service GmbH, Basel, Switzerland). The enclosure provides temperature, humidity, and CO2 gas control to maintain adequate cell culture conditions for the organoids. Organoids were cultured at a constant 37°C, 5% CO2, a humidity flow rate of 25-30 L/hour, and 95-100% relative humidity. Images of the organoids were acquired through the standard microscope software that is capable of automatically acquiring images at different positions, Z-planes/stacks, and multiple fluorescent filters (NIS-Elements software, Japan). The microscope was equipped with a digital complementary metal-oxide semiconductor (CMOS) camera (ORCA-Flash 4.0, Hamamatsu, Japan), which imaged the organoids using a x10 objective at 2 to 4-hour intervals.

Dataset for evaluation of network performance and generalizability

The network structure and training process were manually tuned for performance on the PDAC validation dataset. After optimization, we locked out any further changes to all hyperparameters and evaluated final network performance and generalizability on a separate dataset of 28 organoid microscopy images. The dataset included images of organoids derived from PDAC (10), benign colon tumor cells (6), lung epithelia (6), and salivary adenoid cystic carcinoma (6). The images were obtained through brightfield and phase-contrast microscopy from multiple microscopy cores and manually labeled by two independent reviewers.

Network evaluation and retraining on mouse small intestine organoids

19 images of organoids derived from mouse small intestine were obtained and manually segmented. The OrganoID platform was used to segment and identify individual organoids in these images, which were compared to the manually segmented images. For network retraining, the mouse organoid images were randomly split into groups for training (11), validation (4), and testing (4). The training image set was augmented as above to produce 500 images, which were appended to the original training dataset. The OrganoID neural network was then retrained on this expanded training dataset for an additional 20 epochs and evaluated for performance on the test mouse organoid images as well as the original testing images.

Statistical methods for platform validation

Statistical analysis was performed with the `numpy` and `scipy` packages in Python. Network performance on the testing dataset was evaluated as the pixel-wise intersection-over-union (IOU) of predictions compared to ground-truth segmentations. A single IOU value was computed for each prediction/ground-truth pair and summarized as a mean IOU and standard deviation over the dataset. For agreement of single-organoid counts and measurements, the

Lin concordance correlation coefficient (CCC) was computed as:

$$CCC = \frac{2s_{xy}}{s_x^2 + s_y^2 + (\bar{x} - \bar{y})^2}$$

The Fisher transformation ($arctanh(CCC)$) and its inverse ($tanh(z_{lo}, z_{hi})$) were also used to obtain a z-value and construct a 95% confidence interval for CCC statistics. Effect sizes were computed with Cohen's d statistic:

$$d = \frac{2(M_1 - M_2)}{\sqrt{\sigma_1^2 + \sigma_2^2}}$$

All plots were generated with the `matplotlib` and `seaborn` packages in Python.

Drug screening experiments

PDAC organoids were grown for one week in standard culture conditions and then treated with gemcitabine hydrochloride (G6423, Sigma) at six serial dilutions from 3 nM to 1000 nM with negative control. Propidium iodide (Thermo Fisher P3566) was used to fluorescently measure cellular death and relative viability of organoids in real-time at 4-hour intervals over 72 hours. An MTS proliferation assay (Promega, G3580) was also performed at the end of the experiment to determine cell viability for each condition according to manufacturer's instructions. Statistical hypothesis testing was performed with `scipy` and MATLAB. Organoid circularity was computed as the circumference of a circle with equivalent area divided by the actual perimeter of the organoid.

Validation rigor and indications of robustness

The OrganoID neural network was tested on images of four types of organoids taken at multiple microscopy cores. Images were manually segmented by two independent evaluators. OrganoID single-organoid count and area measurements were compared against the corre-

sponding measurements of the manual test segmentations. OrganoID tracking results were compared to manually tracked images. The OrganoID platform and test microscopy images were distributed to an independent user to confirm reproducibility of all metrics, statistics, and figures.

3.7 References

1. Kretzschmar, K. & Clevers, H. Organoids: Modeling Development and the Stem Cell Niche in a Dish. *Developmental Cell* **38.** Publisher: Elsevier BV, 590–600. ISSN: 1534-5807. http://dx.doi.org/10.1016/j.devcel.2016.08.014 (Sept. 2016).

2. Driehuis, E. *et al.* Oral Mucosal Organoids as a Potential Platform for Personalized Cancer Therapy. *Cancer Discovery* **9.** Publisher: American Association for Cancer Research (AACR), 852–871. ISSN: 2159-8274. http://dx.doi.org/10.1158/2159-8290.cd-18-1522 (May 3, 2019).

3. Dutta, D., Heo, I. & Clevers, H. Disease Modeling in Stem Cell-Derived 3D Organoid Systems. *Trends in Molecular Medicine* **23.** Publisher: Elsevier BV, 393–410. ISSN: 1471-4914. http://dx.doi.org/10.1016/j.molmed.2017.02.007 (May 2017).

4. Sachs, N. *et al.* A Living Biobank of Breast Cancer Organoids Captures Disease Heterogeneity. *Cell* **172.** Publisher: Elsevier BV, 373–386.e10. ISSN: 0092-8674. http://dx.doi.org/10.1016/j.cell.2017.11.010 (Jan. 2018).

5. Clevers, H. & Tuveson, D. A. Organoid Models for Cancer Research. *Annual Review of Cancer Biology* **3.** Publisher: Annual Reviews, 223–234. ISSN: 2472-3428. http://dx.doi.org/10.1146/annurev-cancerbio-030518-055702 (Mar. 4, 2019).

6. Van der Vaart, J. *et al.* Modelling of primary ciliary dyskinesia using patient-derived airway organoids. *EMBO reports* **22.** ISSN: 1469-221X, 1469-3178. https://onlinelibrary.wiley.com/doi/10.15252/embr.202052058 (2022) (Dec. 6, 2021).

7. Richards, D. J. *et al.* Human cardiac organoids for the modelling of myocardial infarction and drug cardiotoxicity. *Nature Biomedical Engineering* **4,** 446–462. ISSN: 2157-846X. http://www.nature.com/articles/s41551-020-0539-4 (2022) (Apr. 2020).

8. Garreta, E. *et al.* Rethinking organoid technology through bioengineering. *Nature Materials* **20.** Publisher: Springer Science and Business Media LLC, 145–155. ISSN: 1476-1122. http://dx.doi.org/10.1038/s41563-020-00804-4 (Nov. 16, 2020).

9. Pettinato, G. *et al.* Spectroscopic label-free microscopy of changes in live cell chromatin and biochemical composition in transplantable organoids. *Science advances* **7.** Publisher: American Association for the Advancement of Science, eabj2800. ISSN: 2375-2548. PMID: 34407934. https://pubmed.ncbi.nlm.nih.gov/34407934 (Aug. 18, 2021).

10. Mead, B. E. *et al.* Screening for modulators of the cellular composition of gut epithelia via organoid models of intestinal stem cell differentiation. *Nature Biomedical Engineering.* ISSN: 2157-846X. https://doi.org/10.1038/s41551-022-00863-9 (Mar. 21, 2022).

11. Brandenberg, N. *et al.* High-throughput automated organoid culture via stem-cell aggregation in microcavity arrays. *Nature Biomedical Engineering* **4,** 863–874. ISSN: 2157-846X. http://www.nature.com/articles/s41551-020-0565-2 (2022) (Sept. 2020).

12. Zhou, Z. *et al.* An organoid-based screen for epigenetic inhibitors that stimulate antigen presentation and potentiate T-cell-mediated cytotoxicity. *Nature Biomedical Engineering* **5,** 1320–1335. ISSN: 2157-846X. https://www.nature.com/articles/s41551-021-00805-x (2022) (Nov. 2021).

13. Wiedenmann, S. *et al.* Single-cell-resolved differentiation of human induced pluripotent stem cells into pancreatic duct-like organoids on a microwell chip. *Nature Biomedical*

Engineering **5,** 897–913. ISSN: 2157-846X. https://www.nature.com/articles/s41551-021-00757-2 (2022) (Aug. 2021).

14. Tanaka, N. *et al.* Three-dimensional single-cell imaging for the analysis of RNA and protein expression in intact tumour biopsies. *Nature Biomedical Engineering* **4,** 875–888. ISSN: 2157-846X. http://www.nature.com/articles/s41551-020-0576-z (2022) (Sept. 2020).

15. Kim, S. *et al.* Comparison of Cell and Organoid-Level Analysis of Patient-Derived 3D Organoids to Evaluate Tumor Cell Growth Dynamics and Drug Response. *SLAS discovery : advancing life sciences R & D* **25.** Edition: 2020/04/30 Publisher: SAGE Publications, 744–754. ISSN: 2472-5560. PMID: 32349587. https://pubmed.ncbi.nlm.nih.gov/32349587 (Aug. 2020).

16. Dekkers, J. F. *et al.* High-resolution 3D imaging of fixed and cleared organoids. *Nature Protocols* **14.** Publisher: Springer Science and Business Media LLC, 1756–1771. ISSN: 1754-2189. http://dx.doi.org/10.1038/s41596-019-0160-8 (May 3, 2019).

17. Hof, L. *et al.* Long-term live imaging and multiscale analysis identify heterogeneity and core principles of epithelial organoid morphogenesis. *BMC biology* **19.** Publisher: BioMed Central, 37–37. ISSN: 1741-7007. PMID: 33627108. https://pubmed.ncbi.nlm.nih.gov/33627108 (Feb. 24, 2021).

18. Bailey, S. R. & Maus, M. V. Gene editing for immune cell therapies. *Nature Biotechnology* **37.** Publisher: Springer Science and Business Media LLC, 1425–1434. ISSN: 1087-0156. http://dx.doi.org/10.1038/s41587-019-0137-8 (June 3, 2019).

19. Ang, L. T. *et al.* A Roadmap for Human Liver Differentiation from Pluripotent Stem Cells. *Cell reports* **22,** 2190–2205. ISSN: 2211-1247. PMID: 29466743. https://pubmed.ncbi.nlm.nih.gov/29466743 (Feb. 20, 2018).

20. Riss, T. & Trask Jr, O. J. Factors to consider when interrogating 3D culture models with plate readers or automated microscopes. *In vitro cellular & developmental biology. Animal* **57.** Edition: 2021/02/09 Publisher: Springer US, 238–256. ISSN: 1543-706X. PMID: 33564998. https://pubmed.ncbi.nlm.nih.gov/33564998 (Feb. 2021).

21. Borten, M. A., Bajikar, S. S., Sasaki, N., Clevers, H. & Janes, K. A. Automated brightfield morphometry of 3D organoid populations by OrganoSeg. *Scientific reports* **8.** Publisher: Nature Publishing Group UK, 5319–5319. ISSN: 2045-2322. PMID: 29593296. https://pubmed.ncbi.nlm.nih.gov/29593296 (Mar. 28, 2018).

22. Kassis, T., Hernandez-Gordillo, V., Langer, R. & Griffith, L. G. OrgaQuant: Human Intestinal Organoid Localization and Quantification Using Deep Convolutional Neural Networks. *Scientific reports* **9.** Publisher: Nature Publishing Group UK, 12479–12479. ISSN: 2045-2322. PMID: 31462669. https://pubmed.ncbi.nlm.nih.gov/31462669 (Aug. 28, 2019).

23. Kok, R. N. U. *et al.* OrganoidTracker: Efficient cell tracking using machine learning and manual error correction. *PloS one* **15.** Publisher: Public Library of Science, e0240802–e0240802. ISSN: 1932-6203. PMID: 33091031. https://pubmed.ncbi.nlm.nih.gov/33091031 (Oct. 22, 2020).

24. Larsen, B. M. *et al.* A pan-cancer organoid platform for precision medicine. *Cell Reports* **36,** 109429. ISSN: 22111247. https://linkinghub.elsevier.com/retrieve/pii/S2211124721008469 (2022) (July 2021).

25. Zhao, N. *et al.* Morphological screening of mesenchymal mammary tumor organoids to identify drugs that reverse epithelial-mesenchymal transition. *Nature communications* **12.** Publisher: Nature Publishing Group UK, 4262–4262. ISSN: 2041-1723. PMID: 34253738. https://pubmed.ncbi.nlm.nih.gov/34253738 (July 12, 2021).

26. Ronneberger, O., Fischer, P. & Brox, T. U-Net: Convolutional Networks for Biomedical Image Segmentation. *Lecture Notes in Computer Science.* Publisher: Springer International Publishing, 234–241. ISSN: 0302-9743. http://dx.doi.org/10.1007/978-3-319-24574-4_28 (2015).

27. Bejani, M. M. & Ghatee, M. A systematic review on overfitting control in shallow and deep neural networks. *Artificial Intelligence Review* **54,** 6391–6438. ISSN: 0269-2821, 1573-7462. https://link.springer.com/10.1007/s10462-021-09975-1 (2022) (Dec. 2021).

28. Clevert, D.-A., Unterthiner, T. & Hochreiter, S. Fast and Accurate Deep Network Learning by Exponential Linear Units (ELUs). Publisher: arXiv Version Number: 5. https://arxiv.org/abs/1511.07289 (2022) (2015).

29. Romero-Calvo, I. *et al.* Human Organoids Share Structural and Genetic Features with Primary Pancreatic Adenocarcinoma Tumors. *Molecular cancer research : MCR* **17.** Edition: 2018/08/31, 70–83. ISSN: 1557-3125. PMID: 30171177. https://pubmed.ncbi.nlm.nih.gov/30171177 (Jan. 2019).

30. Schuster, B. *et al.* Automated microfluidic platform for dynamic and combinatorial drug screening of tumor organoids. *Nature communications* **11.** Publisher: Nature Publishing Group UK, 5271–5271. ISSN: 2041-1723. PMID: 33077832. https://pubmed.ncbi.nlm.nih.gov/33077832 (Oct. 19, 2020).

31. Sachs, N. *et al.* Long-term expanding human airway organoids for disease modeling. *The EMBO journal* **38.** Edition: 2019/01/14 Publisher: John Wiley and Sons Inc., e100300. ISSN: 1460-2075. PMID: 30643021. https://pubmed.ncbi.nlm.nih.gov/30643021 (Feb. 15, 2019).

CHAPTER 4

PROGRAMMABLE DROPLET MICROFLUIDICS FOR COMBINATION SCREENING AND ARRAYED INCUBATION

4.1 Summary

Combination screening is critical for drug discovery, basic research, and precision medicine. Droplet microfluidic devices offer immense throughput for experimental workflows, however droplets produced from a single droplet device will share the same chemical composition. In contrast, valve-based microfluidic devices can be used to precisely control reagent mixtures, yet rely on static on-chip chambers that limit throughput. This chapter describes the design and implementation of PicoScreen, a novel microfluidic strategy for high-throughput combination reagent screening. PicoScreen integrates membrane valves with flow-focusing geometry to produce droplets that contain known and controllable mixtures of inlet reagents. Membrane valves are used to further direct the droplets for storage in an ordered grid, which enables measurement over time with microscopy. A valve multiplexing strategy was used to limit the number of control lines needed to operate the device, which was optimized and evaluated with food dye. PicoScreen is an early-stage technology that can have an immense impact on the high-throughput screening space.

4.2 Project Background

A great deal of chemistry and biology is predicated on mixing two components together and observing the result. Two chemicals can be mixed together to assay the spontaneity of a reaction. A drug can be mixed with bacteria to determine resistance or susceptibility. A virus can be mixed with cells to characterize receptor tropism. In some cases, a desired outcome can be observed only when mixing more than two components together, such as with

the addition of a chemical catalyst, an antibiotic resistance inhibitor, or an inflammatory cytokine. Such experiments are often designed to evaluate a specific hypothesis that is based on intuition, insight, or expertise, with careful selection of the components for use. The process of *high-throughput screening* accelerates this scientific method by investigating many hypotheses in tandem [1–4]. In high-throughput screening, sets of biochemical components are added to isolated reaction chambers with varying combinations or concentrations, and the outcomes are measured at one or more time points for each chamber. By executing many experiments at once – tens, thousands, or even millions – large and high-dimensional combination spaces can be explored with efficiency to find screening "hits" that have important (and often desired) effects.

At present, the most commonly used high-throughput screening systems rely on microtiter plates and pipetting robots [3]. Microtiter plates can hold microliters of fluid in arrays of 96, 386, or 1536 isolated wells. Automated multipipette liquid handling systems can load, transfer between, and sample from multiple wells at once. Microplate readers can quantify outcomes based on fluorometric, colorimetric, and luminometric reporter assays. While these systems are indispensable tools for areas such as industrial drug discovery and chemical synthesis, their use in other contexts is hindered by overhead costs and the large quantities of reagents required for microtiter screens [3]. When working with limited sample quantities, such as tumor biopsies, only microliters may be available for screening. In the microtiter format, these volumes correspond to a few hundred wells (or perhaps, at most, one thousand wells), which is often insufficient to screen all relevant conditions with the necessary experimental and biological replicates and controls.

Microfluidic devices, sometimes referred to as microfluidic "chips", manipulate liquids at the scale of microns, in the range of nanoliters to picoliters, and can contain embedded channels and chambers to run many experiments in parallel [5–7]. Additionally, computer-controllable microfluidic valves can be integrated into chips in order to select, mix, pump,

and route reagents following a programmed experimental instructions [5, 8, 9]. As such, microfluidic platforms can recapitulate the operations of microtiter high-throughput screening platforms, with much more effective use of small sample volumes. However, the number of independent and isolated reaction chambers on such devices is fundamentally limited by chip topology and size, resolution of features, hydraulic resistance, and the number of required valve control lines.

Instead of relying on static reaction chambers, devices can be used to compartmentalize samples within an immiscible fluid [10–12]. For example, a sample of bacteria can be flowed through a microfluidic device to meet an opposing stream of oil, which will pinches off the aqueous stream to form uniform and isolated droplets. The use of a surfactant dissolved in the oil prevents droplet coalescence, and droplets can be collected off-chip for incubation and further processing [13]. With the appropriate chip design and flow conditions, droplets can be formed at kilohertz rates, overtaking the number of reaction vessels used in valve-based and microtiter systems within mere seconds. Standard droplet microfluidic devices produce emulsions with identical chemical compositions determined by the sample that is flowed through the device. This architecture is sufficient for the majority of current applications, however screening platforms require additional methods to evaluate several compositions at once.

The two central tasks for droplet-based screening platforms are to (i) produce droplets with varying compositions and (ii) encode or track the contents of each droplet during measurement. Existing platforms approach the first problem through the use of pooled droplet generators [14], braille valves [15], or diffusion gradients [16]. These systems have been thoroughly validated to produce useful results, however they are either unable to make combinations, restricted to a low number of conditions, or scale poorly for high-throughput applications. The second problem is most commonly approached by storing the droplets in a static array [17]. Droplets are either tracked based on order [15] or through fluores-

cence measurements [14]. Fluorescent barcoding strategies add a unique concentration or concentration of fluorophore to each droplet [14], however these approaches are are limited by overlap of fluorescence spectra and the dynamic range and resolution of measurements. Storage in one dimension (e.g. in a length of microbore tubing) scales poorly with the number of conditiosn [15]; this limitation can be overcome with two- or three-dimensional droplet arrays, however existing platforms are low-throughput, low-density, or unordered.

PicoScreen is a high-throughput screening platform that integrates computer-controlled valves into a droplet-based microfluidic chip. The device produces monodisperse emulsions of a sample, and can add any two of ten possible reagents to each droplet. Droplets are stored on-chip in an ordered grid, which is filled row-by-row through actuation of the integrated valves. The chip is optically transparent, which enables microscopy measurements of droplet contents, and programmable with open-source software. PicoScreen is an important step towards the miniaturization of high-throughput screening for economical use in small-volume applications.

4.3 Results

PicoScreen was developed to emulsify a sample in thousands of distinct picoliter droplets with software-controllable chemical compositions and store the droplets in an ordered grid to keep track of conditions during response measurement. The central approach of this platform to integrate membrane valves with a droplet generator to select and dilute pairs of reagents for production of monodisperse droplets with varying contents (Figure 4.1a). The generated droplets are then sent to an incubation grid, which is filled row-by-row under control of several more membrane valves (Figure 4.1b). To enable scaling of the device to a large number of inlet reagents and droplet storage rows, the valves are multiplexed with a combinatorial addressing strategy. While the each reagent and row could instead be controlled by a dedicated valve, the multiplexing approach scales exponentially – for

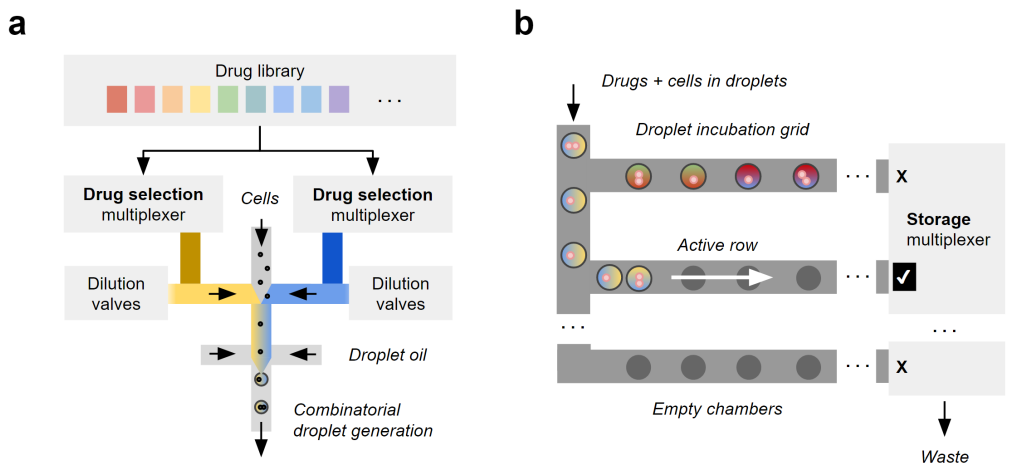

Figure 4.1: The PicoScreen combinatorial droplet screening strategy. (a) A microfluidic device generates droplets with varying and controlled combinations of inlet reagents. Multiplexed membrane valves are used to select pairs of reagents for co-flow in a channel, which is then directed to meet a set of perpendicular oil channels to generate droplets. Additional valves to optionally dilute the reagent pairs are included in the device. (b) To keep track of droplet contents and follow response over time, droplets are stored on-chip in an ordered two-dimensional grid. The grid is filled row-by-row under the control of multiplexed membrane valves, and droplets enter each row in a single-file line. Use of an optically transparent material (polydimethylsiloxane) for the device enables straightforward monitoring with microscopy.

example, one of 1,000 reagent or storage rows can be selected with the use of only 13 valves.

A prototype device was developed to evaluate and optimize the overall valve-controlled droplet generation strategy. In the prototype device, 10 membrane valves control the flow of 10 separate reagents into a shared junction, which is then routed through a flow-focusing droplet generator (Figure 4.2a). The chip was fabricated from PDMS with a standard soft lithography process and bonded to a microscope slide. Evaluation of the combinatorial generation was carried out with food dye. Programmed actuation of the microfluidic valves produced emulsions that corresponded to the selected colors (Figure 4.2b).

Similarly, a prototype device was developed to optimize and validate droplet routing and storage in a microfluidic chip under multiplexed valved control. This device features four valved reagent inlets, which are mixed and directed through a flow-focusing droplet

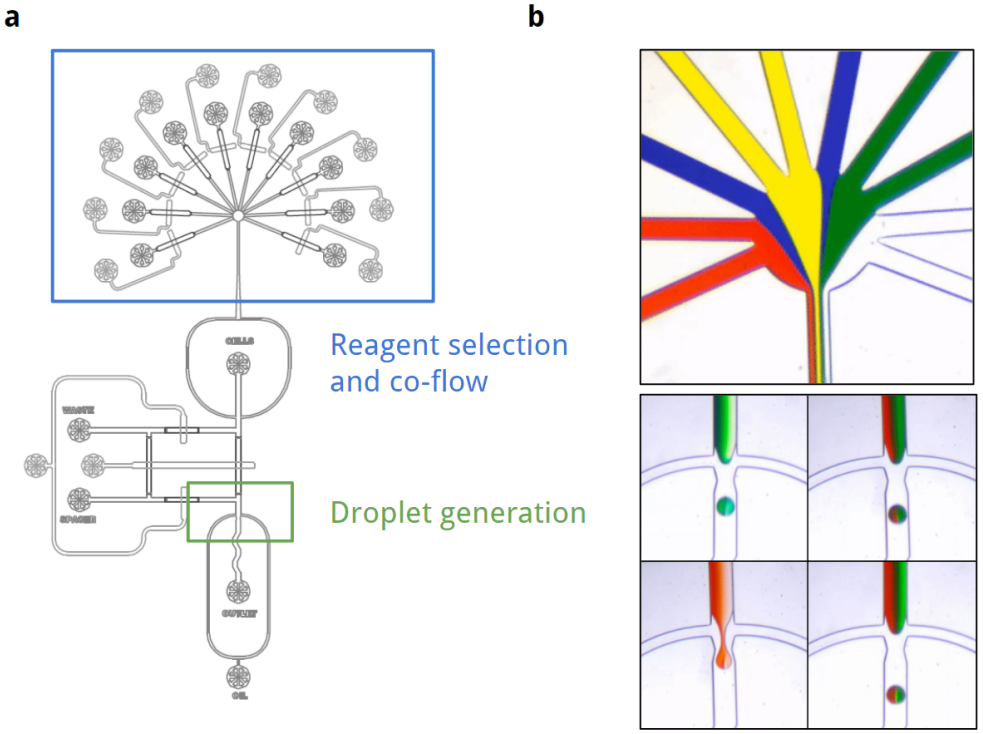

Figure 4.2: A microfluidic device for combinatorial droplet generation. (a) Membrane valves were integrated into a droplet-based microfluidic device fabricated from PDMS to evaluate and optimize the screening strategy. The device featured 10 inlets for reagents, which could be selected with individual valves and co-flowed through a shared channel. The reagent mixture was then directed to flow through a flow-focusing droplet generator to produce monodisperse emulsions in fluorinated oil. This prototype device also included components for flowing in cell sample and discarding waste, however these were not used in validation experiments. (b) Food dye was used to qualitatively validate the device. Shown are microscopy images of the reagent co-flow and droplet generation junctions. The top image shows the device in a state where all reagents are selected. The bottom panel of four images shows droplets generated with distinct mixtures of food dye during other device states.

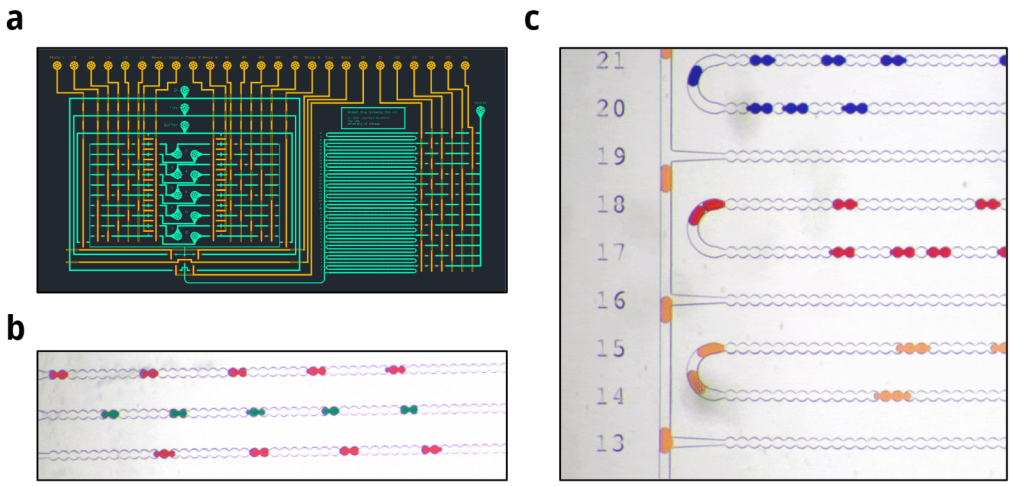

Figure 4.3: An integrated device for droplet screening and ordered storage. (a) The AutoCAD design the PicoScreen microfluidic device features a combinatorial droplet generator to produce mixtures of any pairs of 10 input reagents. The emulsified droplets are then sent to a storage grid, which contains 42 rows for ordered incubation. (b) Food dye was used to validate the droplet storage strategy. The device was programmed to store droplets in sets of 5 replicates. Microscopy revealed between 4 and 6 replicates stored per condition. (c) The droplets are stored in serpentine channels per-row to increase packing.

generator to a storage array. The array contains 50 storage columns under the control of 8 multiplexed valves, as well as a bypass valve to optionally discard droplets. The device was validated with food dye and programmed to store droplets with distinct colors in each column. Brightfield microscopy of the stored droplets confirmed generation and storage of the desired conditions.

The final PicoScreen device integrates a multiplexed droplet generation module with a multiplexed droplet storage model on one chip (Figure 4.3a). The device produces monodisperse emulsions of input sample, and can add any of 52 pairwise combinations of 10 reagents under the control of 10 multiplexed valves. The storage module features 14 independent channels, which are arranged in a serpentine pattern to produce 42 storage rows under the control of 6 valves. The device was again evaluated with food dye to and programmed to store droplets with alternating colors in each row, in replicate sets of 5 droplets (Figure 4.3b-c). While the number of replicate droplets per condition varied between 4 and 6, most

replicates indeed contained 5 droplets and the device was observed to produce the desired pattern.

4.4 Discussion and Future Directions

The PicoScreen platform produces droplets with varying and controlled combinations of reagents in a high-throughput fashion. Conditions are selected through the use of integrated microfluidic membrane valves that mix and route reagents through a droplet generator. The droplets are stored on the chip in an ordered grid, which enables measurement of responses through microscopy over time. Furthermore, the multiplexed valve configuration enables the device design to be scaled to hundreds or thousands of reagents and storage rows.

Control of droplet compositions and ordered storage was validated with food dye and brightfield microscopy. Droplet colors can be easily evaluated by eye for qualitative assessment of performance, however additional validation should be carried our for quantitative metrics. Fluorochrome dyes can be used in place of food dyes and imaged with fluorescence microscopy, and the excitation intensity will be proportional to the dye concentration. This can quantify any contamination across reagent channels or crosstalk between incubated droplets, which are important metrics for use in sensitive applications.

The grid-incubated droplets were seen to evaporate over the course of 2-3 hours, which limits the use of the platform, in its current state, to assays with shorter incubation periods. Mammalian cell responses can take many hours to develop after exposure to a chemical stimulus, so this platform may find more accessible use in cell-free or microbial applications. Protein crystallization has been previously performed in droplets [18], and this process could be adapted in the PicoScreen platform to test many conditions at once. Bacterial samples could be cultured in the device for antibiotic susceptibility testing or interactions with bacteriophages.

Future designs of the PicoScreen chip can include inlets and valves for more reagents

and a larger storage grid. The grid can also be optimized to fit more droplets in each row, such as with hydrodynamic droplet traps [19] or multi-height channel wells [20, 21]. Another possiblity would be to replace the storage grid with a series of large storage chambers that are addressed with a multiplexed valve array, and use a microscope to record droplets as the enter a chamber to track the order of generation. Oil filters integrated into the chamber could ensure that the droplets tightly pack together into a static array, after which the microscope can be directed to the next chamber for loading.

4.5 Methods

4.5.1 Microfluidic device design and fabrication

The PicoScreen chip was designed with AutoCAD software (Autodesk). A custom LISP script was written to automate the arraying of multiplex valves in a combinatorial addressing pattern.

Device molds were fabricated with a standard lithography process [22]. Briefly, silicon wafers were vapor-treated with hexamethyldisilazane to enhance photoresist adhesion. SU-8 3025 photoresist (Kayaku) was spin-coated onto the wafers and UV-exposed with a maskless aligner (Heidelberg MLA150) to rasterize flow and control channels 25 microns in height. AZ 40-XT photoresist (Microchemicals) was spun onto wafers, exposed, and melted at 200C for 13 hours to form features with rounded cross sections for sealable valve junctions.

The molds were used to create multiple devices from polydimethylsiloxane (PDMS, RTV-615, Momentive Performance Materials). Poured PDMS was degassed in a vacuum chamber to remove bubbles and cured at 80C for 1 hour. Access holes for flow and control pins were added with a 1mm biopsy punch (Syneo). Device layers were bonded together and to glass with a plasma cleaner (Harrick) set to high power with 700 mTorr of pure oxygen for 25 seconds. Bonded devices were then baked overnight at 80C. Finally, devices were treated

with Aquapel through the oil inlet pinhole and baked once more at 80C overnight.

4.5.2 Device operation and imaging

Food dye, PBS, and fluorinated oil (Droplet Generation Oil for EvaGreen, Bio-Rad) were added to 2mL microcentrifuge tubes with membrane caps (Sarstedt). Caps were punctured with 1.5-inch blunt-tip needles (McMaster) to connect each reagent to the chip through Tygon tubing and pressurize each tube with air. A digital flow controller (OB1, Elveflow) was used to set precise pressures for each reagent to produce monodisperse droplets (10 psi for oil, 8 psi for buffer/sample, and 7 psi for dyes). Valve pressure tubing was controlled with a solenoid array built in-house and described previously [22] and programmed with custom Python software. Videos and images of droplet generation and storage were obtained with a benchtop inverted brightfield microscope (Leica) and a high-frame-rate camera (Basler).

4.6 References

1. M. Payne, E., A. Holland-Moritz, D., Sun, S. & T. Kennedy, R. High-throughput screening by droplet microfluidics: perspective into key challenges and future prospects. en. *Lab on a Chip* **20.** Publisher: Royal Society of Chemistry, 2247–2262. `https://pubs.rsc.org/en/content/articlelanding/2020/lc/d0lc00347f` (2023) (2020).

2. Hertzberg, R. P. & Pope, A. J. High-throughput screening: new technology for the 21st century. en. *Current Opinion in Chemical Biology* **4,** 445–451. ISSN: 1367-5931. `https://www.sciencedirect.com/science/article/pii/S1367593100001101` (2023) (Aug. 2000).

3. Zeng, W., Guo, L., Xu, S., Chen, J. & Zhou, J. High-Throughput Screening Technology in Industrial Biotechnology. en. *Trends in Biotechnology* **38,** 888–906. ISSN: 0167-7799.

https://www.sciencedirect.com/science/article/pii/S0167779920300019 (2023) (Aug. 2020).

4. Mayr, L. M. & Bojanic, D. Novel trends in high-throughput screening. en. *Current Opinion in Pharmacology. Anti-infectives/New technologies* **9,** 580–588. ISSN: 1471-4892. https://www.sciencedirect.com/science/article/pii/S1471489209001283 (2023) (Oct. 2009).

5. Melin, J. & Quake, S. R. Microfluidic Large-Scale Integration: The Evolution of Design Rules for Biological Automation. *Annual Review of Biophysics and Biomolecular Structure* **36.** _eprint: https://doi.org/10.1146/annurev.biophys.36.040306.132646, 213–231. https://doi.org/10.1146/annurev.biophys.36.040306.132646 (2023) (2007).

6. Whitesides, G. M. The origins and the future of microfluidics. en. *Nature* **442.** Number: 7101 Publisher: Nature Publishing Group, 368–373. ISSN: 1476-4687. https://www.nature.com/articles/nature05058 (2023) (July 2006).

7. Banik, S. *et al.* The revolution of PDMS microfluidics in cellular biology. *Critical Reviews in Biotechnology* **43,** 465–483. ISSN: 0738-8551. https://doi.org/10.1080/07388551.2022.2034733 (2023) (Apr. 2023).

8. Unger, M. A., Chou, H.-P., Thorsen, T., Scherer, A. & Quake, S. R. Monolithic Microfabricated Valves and Pumps by Multilayer Soft Lithography. *Science* **288.** Publisher: American Association for the Advancement of Science, 113–116. https://www.science.org/doi/full/10.1126/science.288.5463.113 (2023) (Apr. 2000).

9. Cole, M. C., Desai, A. V. & Kenis, P. J. A. Two-layer multiplexed peristaltic pumps for high-density integrated microfluidics. en. *Sensors and Actuators B: Chemical* **151,** 384–393. ISSN: 0925-4005. https://www.sciencedirect.com/science/article/pii/S0925400510005873 (2023) (Jan. 2011).

10. Shang, L., Cheng, Y. & Zhao, Y. Emerging Droplet Microfluidics. *Chemical Reviews* **117.** Publisher: American Chemical Society, 7964–8040. ISSN: 0009-2665. https://doi.org/10.1021/acs.chemrev.6b00848 (2023) (June 2017).

11. Joensson, H. N. & Andersson Svahn, H. Droplet Microfluidics—A Tool for Single-Cell Analysis. en. *Angewandte Chemie International Edition* **51,** 12176–12192. ISSN: 1521-3773. https://onlinelibrary.wiley.com/doi/abs/10.1002/anie.201200460 (2023) (2012).

12. T. Guo, M., Rotem, A., A. Heyman, J. & A. Weitz, D. Droplet microfluidics for high-throughput biological assays. en. *Lab on a Chip* **12.** Publisher: Royal Society of Chemistry, 2146–2155. https://pubs.rsc.org/en/content/articlelanding/2012/lc/c2lc21147e (2023) (2012).

13. Baret, J.-C. Surfactants in droplet-based microfluidics. en. *Lab on a Chip* **12.** Publisher: The Royal Society of Chemistry, 422–433. ISSN: 1473-0189. https://pubs.rsc.org/en/content/articlelanding/2012/lc/c1lc20582j (2023) (Jan. 2012).

14. Kulesa, A., Kehe, J., Hurtado, J. E., Tawde, P. & Blainey, P. C. Combinatorial drug discovery in nanoliter droplets. en. *Proceedings of the National Academy of Sciences* **115,** 6685–6690. ISSN: 0027-8424, 1091-6490. https://pnas.org/doi/full/10.1073/pnas.1802233115 (2023) (June 2018).

15. Eduati, F. *et al.* A microfluidics platform for combinatorial drug screening on cancer biopsies. en. *Nature Communications* **9.** Number: 1 Publisher: Nature Publishing Group, 2434. ISSN: 2041-1723. https://www.nature.com/articles/s41467-018-04919-w (2023) (June 2018).

16. Miller, O. J. *et al.* High-resolution dose–response screening using droplet-based microfluidics. *Proceedings of the National Academy of Sciences* **109.** Publisher: Proceedings of

the National Academy of Sciences, 378–383. https://www.pnas.org/doi/10.1073/pnas.1113324109 (2023) (Jan. 2012).

17. Pompano, R. R., Liu, W., Du, W. & Ismagilov, R. F. Microfluidics using spatially defined arrays of droplets in one, two, and three dimensions. eng. *Annual Review of Analytical Chemistry (Palo Alto, Calif.)* **4,** 59–81. ISSN: 1936-1335 (2011).

18. Li, L. & Ismagilov, R. F. Protein Crystallization Using Microfluidic Technologies Based on Valves, Droplets, and SlipChip. *Annual Review of Biophysics* **39,** 139–158. https://doi.org/10.1146/annurev.biophys.050708.133630 (2023) (2010).

19. Han, S. H., Kim, J. & Lee, D. Static array of droplets and on-demand recovery for biological assays. *Biomicrofluidics* **14,** 051302. ISSN: 1932-1058. https://doi.org/10.1063/5.0022383 (2023) (Sept. 2020).

20. Labanieh, L., Nguyen, T., Zhao, W. & Kang, D.-K. Floating Droplet Array: An Ultra High-Throughput Device for Droplet Trapping, Real-time Analysis and Recovery. en. *Micromachines* **6,** 1469–1482. ISSN: 2072-666X. http://www.mdpi.com/2072-666X/6/10/1431 (2023) (Sept. 2015).

21. Duchamp, M. *et al.* Microfluidic Device for Droplet Pairing by Combining Droplet Railing and Floating Trap Arrays. *Micromachines* **12,** 1076. ISSN: 2072-666X. https://www.ncbi.nlm.nih.gov/pmc/articles/PMC8470175/ (2023) (Sept. 2021).

22. Schuster, B. *et al.* Automated microfluidic platform for dynamic and combinatorial drug screening of tumor organoids. *Nature communications* **11.** Publisher: Nature Publishing Group UK, 5271–5271. ISSN: 2041-1723. PMID: 33077832. https://pubmed.ncbi.nlm.nih.gov/33077832 (Oct. 19, 2020).

CHAPTER 5

COMPREHENSIVE COMBINATION SCREENING OF TRANSCRIPTOMIC RESPONSES IN INDIVIDUAL CELLS

5.1 Summary

Combination therapy is a powerful strategy to combat drug resistance, as a cancer cell is presumably less likely to be resistant to multiple drugs at once. A major challenge is to sieve this enormous treatment set to identify the most effective regimens. High-throughput screening platforms can investigate many treatments on cell-free, *in vitro*, or *ex vivo* disease models; however, the measured outputs are often insufficient to capture the nuanced molecular processes that can be manipulated for treatment. This chapter describes a screening platform, Screen-seq, that is high-throughput, high-content, and practical for biomedical research and per-patient use. Screen-seq efficiently measures the rich transcriptomic responses of thousands of individual cells to each possibility in the complete combination space of several reagents. A novel microfluidic strategy combines flow-focusing geometry with computer-controlled membrane valves to emulsify cells in droplets with precise and diverse mixtures of inlet solutions with the appropriate negative controls. The cell treatment and recovery process was optimized to maintain compatibility with single-cell sequencing workflows. Synthetic oligonucleotides conjugated to universal antibodies flexibly barcode each reagent so that conditions can be decoded alongside the transcriptome. The microfluidic device was preliminarily validated with fluorophores, and the entire screening platform was validated through the use of a predefined set of experimental conditions that were correctly captured in sequencing. Screen-seq serves as a powerful platform for translational research and precision therapy to improve outcomes for cancer patients.

5.2 Project Background

Cancer cells can thrive through redundant molecular pathways and exist in a heterogeneous population within a given tumor [1, 2]. As such, combination therapy is a central approach in drug treatment to target multiple pathways at once and limit the emergence of drug resistance through unresponsive subpopulations [3, 4]. However, there is an incredibly broad set of drugs that have been developed to treat the various molecular and histological types of cancer and, accordingly, and even broader set of combination therapies that are possible. While clinical trials can provide valuable insight into the comparative benefits and risks of a treatment regimen on a patient population, it is impossible to comprehensively cover the space of possible treatments due to practical limitations of cost and number of cases. Instead, *in vitro* screening methods are often used to refine the list of possibilities to the most promising options, which can then be evaluated through clinical studies [5, 6]. Most high-throughput screening platforms are based on cell lines cultivated in microtiter plates and scalar colorimetric, fluorometric, or luminometric report assays [7–9]. These technologies are critical for target-based drug discovery, however the reporters can fail to capture important cellular responses and provide low-dimensional insight into the mechanism of action of the agents that are tested. Furthermore, microtiter cell-based screening platforms measure the average response of many cultured cells per condition, which can fail to capture sample heterogeneity.

Single-cell RNA sequencing (scRNA-seq) methods can supplement these technologies, measuring detailed transcriptomic responses at the level of individual cells [10–12]. Furthermore, droplet-based microfluidic devices can be used for scRNA-seq to offer immense throughput, with the ability to profile thousands of cells in a single assay [13, 14]. However, standard droplet generators produce droplets with identical chemical compositions determined solely by the input sample. Additional steps and tools must be used to compare the responses of differentially stimulated populations.

A number of methods have been developed to investigate transcriptomic responses of single cells to different combinations of reagents in droplets [15, 16]. These platforms are impressively designed and rigorously validated, however they are, fundamentally, restricted to the investigation of reagent pairs. Most combination therapies include three or more drugs [3]. Consequently, screening such regimens requires an additional level of control to produce higher-order drug combinations.

Valve-based microfluidic devices can include embedded cell culture chambers and offer exquisite control of chemical environments [17, 18]. However, the number of conditions that can be explore is, here, restricted by the number of chambers that can fit onto a single chip, which can produce insurmountably high hydrodynamic resistance for large devices. A combination of droplet microfluidics and valve-based microfluidics has the possibility of retaining the best of both. The platform discussed in the previous chapter, PicoScreen, is a novel example of how chip-integrated valves can be combined with a droplet generator in a single chip to screen responses through imaging.

This chapter introduces a new platform, called Screen-seq, that adapts and extends components of PicoScreen to again perform high-throughput droplet screening, but now with scRNA-seq as the endpoint measurement of cellular responses. The microfluidic device designed for Screen-seq produces monodisperse emulsions of cells in media, and can add any combination of 8 distinct reagents to each droplet under software control. The chip also includes channels for 8 negative controls, paired with each reagent inlet. The Screen-seq protocol uses reagent-specific oligonucleotide labels to encode droplet contents on each cell, and was optimized for compatibility with downstream scRNA-seq. This strategy enables simultaneous decoding of screening conditions alongside the transcriptome of each cell. The Screen-seq platform offers a level of throughput and content that is unprecedented at the single-cell level, which will facilitate deeper insights into the mechanisms of combination therapies and the identification of ideal regimens per-patient.

5.3 Design and Implementation

5.3.1 A microfluidic device for rapid generation of controlled droplet mixtures

The Screen-seq platform relies on a novel microfluidic device that encapsulates cells in picoliter droplets with varying and programmable combinations of 8 reagent inlets (Figure 5.1). Cell samples, screening reagents, and fluorinated oil with surfactant are prepared in microcentrifuge tubes, connected to the device through microbore tubing, and pressurized with air to drive fluids into the respective channels. Membrane valve control channels are also connected to air pressure that is controlled by electronic solenoid valves to select any of the 256 possible reagent via custom automation software. The device co-flows the selected reagents together and with the cell sample before passing through a flow-focusing droplet generator to produce a monodisperse emulsion. The droplets are transferred off-chip into a microcentrifuge tube for bulk incubation of cellular responses.

Cellular responses to particular reagents must be compared to the appropriate negative control, and each reagent may be dissolved in a different buffer, such as pure PBS or diluted DMSO, that could induce confounding effects on measurements. Accordingly, each reagent channel is paired with an additional flow channel to carry the corresponding negative control buffer (sometimes referred to as the *vehicle* for the reagent). The reagent/vehicle channel pairs are controlled by membrane valves that are programmed to actuate in opposition to one another. With this strategy, there are always exactly 8 active fluid channels that mix with the sample channel and each droplet will be composed of the same buffer, regardless of the number of selected reagents.

Microfluidic membrane valves can actuate with response times as fast as 10 milliseconds. However, once a valve is opened, the released fluid must propagate through the flow channel, which can take several seconds (or even minutes), depending on the hydraulic resistance of

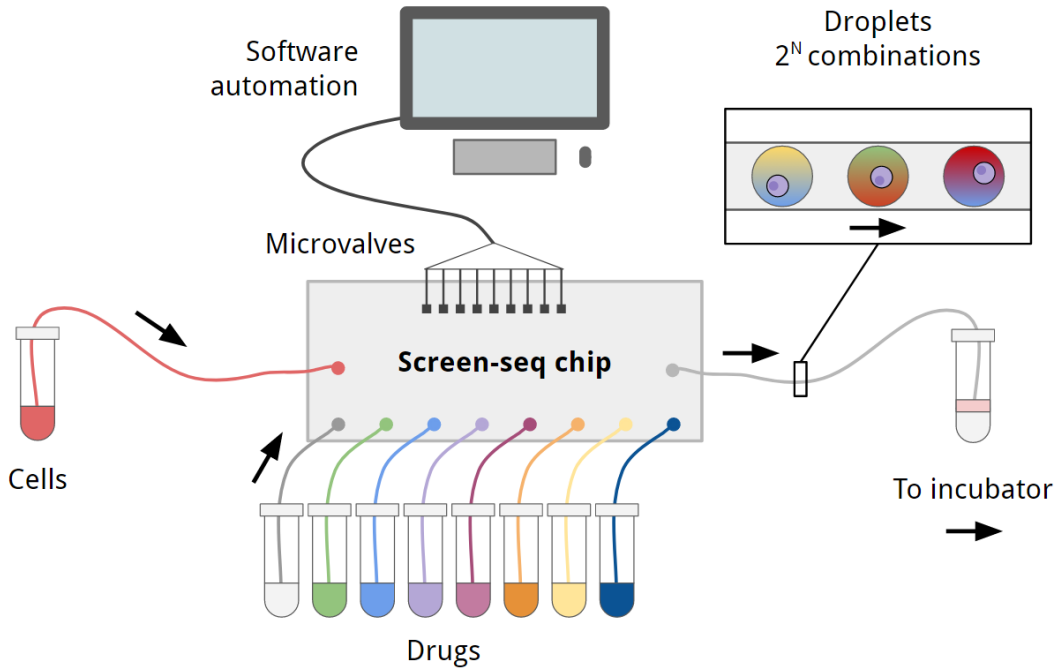

Figure 5.1: Screen-seq microfluidic workflow. The Screen-seq platform uses a novel microfluidic device to produce droplet emulsions of cells with any possible combination of inlet drugs or reagents. Integrated membrane valves are used to select reagent combinations under software control. Droplets are collected off-chip and transferred to an incubator to enable maturation of cellular responses.

the system. During this period, the leading edge of the fluid stream will diffuse into the existing contents of the channel, producing a concentration gradient. This diffusion process is accelerated by Taylor-Aris dispersion [19], whereby shear stresses within the channel walls increase the effective diffusion coefficient of the fluid species. When the valves in the Screen-seq chip are actuated to select a new combination of reagents, the reagents take 1-2 seconds to propagate to the droplet generation junction. While this delay may seem insignificant at first glance, it is large in comparison to the droplet generation rate – approximately 200 Hz for the Screen-seq chip. As such, hundreds of droplets are generated in this interval, with concentrations that transition gradually to the new steady-state configuration. To ensure that each collected droplet contains the precise combination of reagents dictated by the control software, the Screen-seq chip also includes a valve-actuated sorting junction that discards droplets during the transition window (Figure 5.3e).

5.3.2 Encoding droplet contents with antibody-oligonucleotide conjugates

While the Screen-seq microfluidic device can produce droplets with different chemical compositions, the contents of each droplet must be somehow encoded so that responses can be matched to the droplet conditions. Screen-seq uses a molecular strategy based on cell hashing [20] to attach synthetic oligonucleotides to each cell that describe the environment of each cell's droplet (Figure 5.2). Namely, each oligonucleotide contains a sequence (referred to here as a *barcode*) that is specific to each reagent. The oligonucleotides are conjugated to an antibody that binds to a surface receptor universally expressed by cells in the sample of interest. These barcode conjugates are premixed with their respective reagents prior to the Screen-seq protocol at a fixed concentrations, so that generated droplets will contain a barcode mixture that corresponds to the reagent mixture. Inside of the droplet, the antibodies will attach to the surface of the cell, effectively encoding the contents of the droplet on the cell surface. Each reagent channel is paired with a vehicle channel that serves as a negative

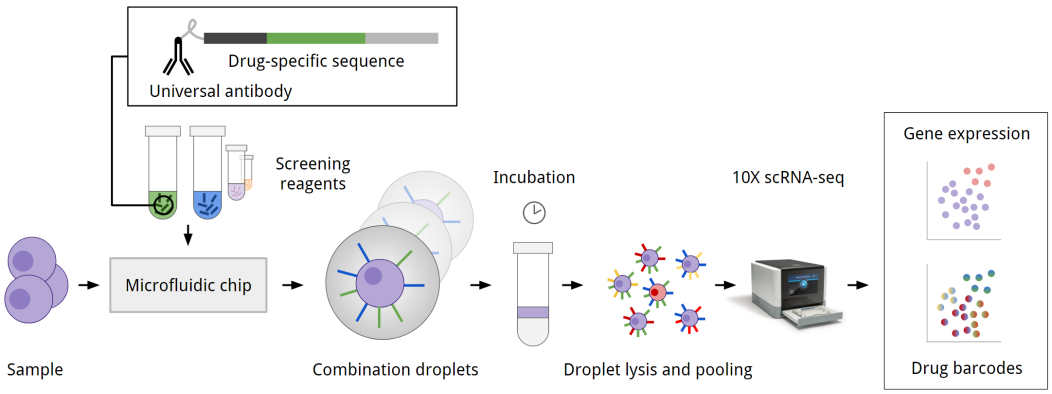

Figure 5.2: Screen-seq cell barcoding workflow. The Screen-seq platform uses a molecular barcoding strategy to encode the composition of each droplet onto the surface of treated cells. Antibody-oligonucleotide conjugates are synthesized to bind to surface proteins universally expressed by cells in the sample and premixed with each reagent. The oligonucleotides contain a known base sequence "barcode" that is specific to each reagent, however the antibody is shared across all reagents. With this strategy, the generated droplets will contain mixtures of barcode conjugates that correspond to the reagent mixture, and will adhere to cell surfaces, encoding contents. Droplets are pooled and incubated in bulk, and then lysed to release the intact cells. These cells can be profiled with commercial single-cell RNA sequencing platforms to measure gene expression alongside reagent barcodes, to uncover relationships between reagent combinations and cell states.

control; as such, the vehicles are also be premixed with a barcode conjugate. This strategy not only maintains experimental validity, but also accounts for variations in the number of surface receptors per cell.

5.3.3 Intefacing with single-cell RNA sequencing

The Screen-seq platform was designed for compatibility with 10X Genomics scRNA-seq systems. For 10X sequencing, cells must be prepared in a compatible buffer and at a precise concentration to minimize the likelihood of chip clogs or cell multiplets. Accordingly a critical step in the Screen-seq pipeline is to extract cells from the droplets after incubation while preserving viability and membrane integrity. Droplets can be broken with perfluorooctanol (PFO), which sequesters fluorosurfactants to destabilize the droplet interface and encourage coalescence. However, PFO is also highly toxic and will rapidly disintegrate cell membranes

[21]. This risk is particularly problematic as cell recovery and washing requires centrifugation – PFO and mammalian cells are both much denser than water and will collect together at the bottom of the tube.

Density gradient media was mixed with all reagents prior to encapsulation to increase the density of droplet contents beyond the mass density of a typical cell. Through this strategy, the cells released by a droplet upon PFO addition will instead collect at the top of the centrifuge tube, opposite to the PFO (which remains much denser than the media). After droplet lysis, the released media and cells can be transfered to a new tube and mixed with a lower-density buffer to allow proper cell pelleting and washing.

5.4 Results

5.4.1 Screen-seq generates droplets with distinct and consistent compositions

The Screen-seq chip was first qualitatively validated with food dye to determine appropriate operating parameters (Figure 5.3). The dyes were then replaced with fluorochrome dyes to quantitatively assess performance. The chip was programmed to produce droplets with compositions that alternated between fluorescein or PBS, and to discard droplets over a 5-second transition window. The collected droplets were then imaged with brightfield and fluorescence microscopy, and the total fluorescence per droplet was quantified with automated brightfield segmentation (Figure 5.4a). The analysis indeed revealed two separate populations of droplets with low and high levels of fluorescein, corresponding to the programmed conditions, with no droplets of intermediate fluorescence (Figure 5.4b). Resorufin, a fluorochrome dye with an excitation and emission spectrum distinct from fluorescein, was used to measure the degree of channel contamination and droplet crosstalk over time. The chip was programmed to now produce droplets with contents that alternated between PBS, fluorescein, or resorufin, again with a 5-second discard window. The collected droplets were

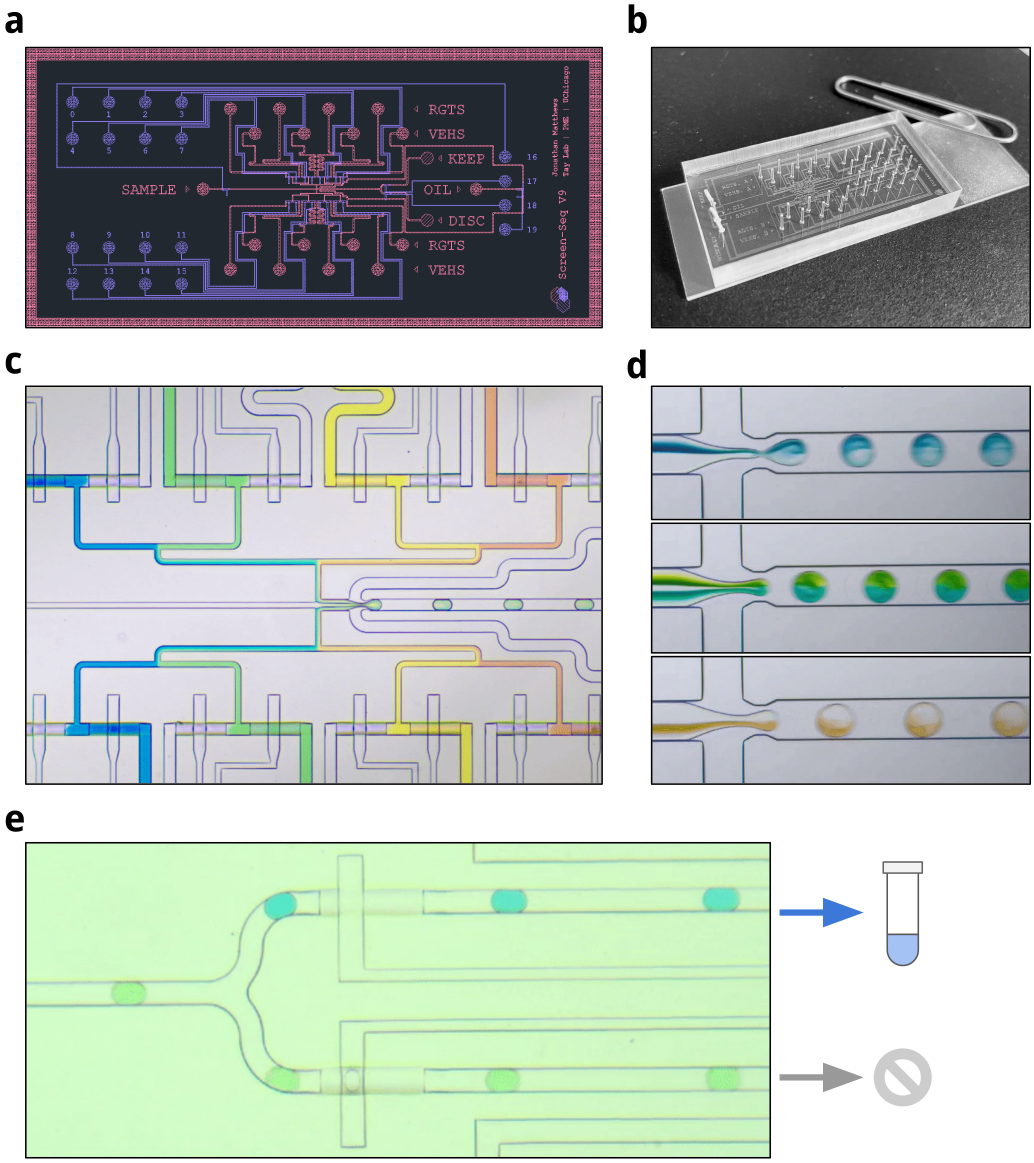

Figure 5.3: The Screen-seq microfludic device. (a) The AutoCAD design for the Screen-seq device, which includes inlets for 8 reagents and negative controls, as well as cell sample and oil, altogether controlled by 20 integrated microfluidic valves. (b) The device was fabricated from PDMS with a soft lithography method. (c) Brightfield microscopy image of the droplet generation junction, showing food dye in the 8 reagent channels co-flowing to meet channels of sample and oil. (d) The valves can be actuated to control the contents of droplets according to a programmed software experiment. Shown are representative images of droplets produced during a mock screening experiment. (e) A sorting junction was designed on the chip to enable time-based discarding of droplets during condition stabilization.

then imaged, incubated for 24 hours, and imaged once more in brightfield and fluoresence microscopy. The fluorescence measurements of the immediately-imaged droplets demonstrated 3 distinct populations that corresponded to droplets with high- and low- levels of fluorescein or resorufin, with no droplets of intermediate or mixed levels (Figure 5.4c). However, measurements of the incubated droplets revealed only one population for the resorufin channel, indicating considerable crosstalk via diffusion of resorufin between droplets over time. In contrast, two distinct populations were still observed in the fluorescein channel, which suggests that the crosstalk is reagent-dependent, and matches existing literature [22, 23]. Overall, these fluorescence results indicate that the Screen-seq chip can indeed produce droplets with precise and controlled combinations of multiple reagents.

5.4.2 Screen-seq integrates with single-cell RNA sequencing

Compatibility with 10X scRNA-seq pipelines was evaluated with K562 cells, a leukemia cell line. Anti-CD298 universal antibodies were used to attach barcodes to each cell, which was validated for the K562 cells with flow cytometry (Figure 5.5). Cell media was density-matched to K562 cells, which were then encapsulated into droplets with the Screen-seq chip, along with various combinations of barcodes dissolved in PBS. Collected droplets were incubated for 16 hours at 37C and then lysed. Viability of the recovered cells was then measured with an MTS assay and determined to be 168% of that of the initial sample. This expansion suggests cell proliferation, which aligns well with the approximate 20-hour doubling time reported for K562 cells. Recovered cells were washed and sequenced with a 10X scRNA-seq protocol. Analysis of the sequencing results showed capture of 5,808 high-quality cells that clustered into 15 groups of transcriptomic heterogeneity (Figure 5.6a). The gene with the highest differential expression across clusters was HBZ, which codes for the hemoglobin-ζ protein subunit (Figure 5.6b-c). Encouragingly, HBZ has been previously identified to be overexpressed in populations of K562 cells [24–26]. These results support

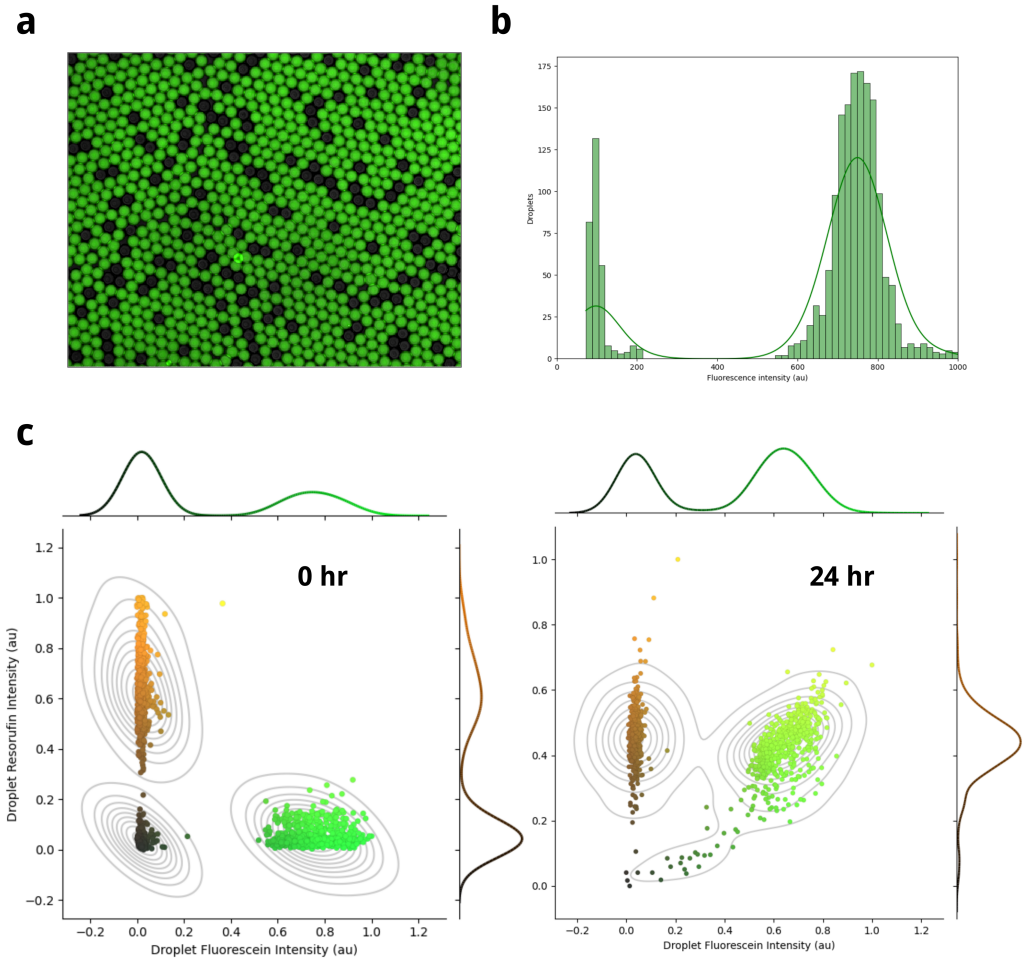

Figure 5.4: Fluorescence validation of the Screen-seq device. (a) Droplets were programmed to contain either PBS or fluorescein, a green-fluorochromic dye. Shown are a sample of droplets imaged in a monolayer on a hemocytometer. (b) Quantification of the total fluorescein intensity per droplet showed two distinct populations, matching the generation program. No droplets were observed in between the two populations, which indicates desired operation of the sorting junction. (c) A second fluorochromic dye, resorufin (orange), was used to measure channel contamination and droplet crosstalk. The device was programmed to produce droplets that contained either PBS, resorufin, or fluorescein. Analysis of immediately-sampled droplets revealed three distinct populations that corresponded to the programmed conditions. Analysis of the same droplets 24 hours later showed crosstalk of resorufin, yet maintenance of the two fluorescein populations.

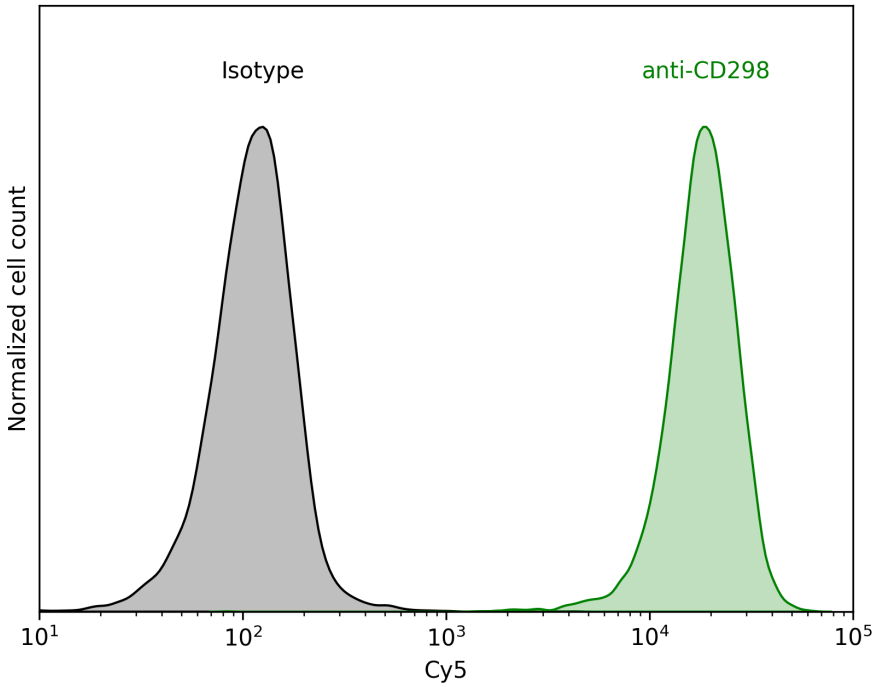

Figure 5.5: Flow cytometry of anti-CD298 universal antibodies. Anti-CD298 universal antibodies were purchased from BioLegend and conjugated to a Cy5 fluorophore in-house. These were confirmed to bind to K562 cells through flow cytometry when compared to an isotype control.

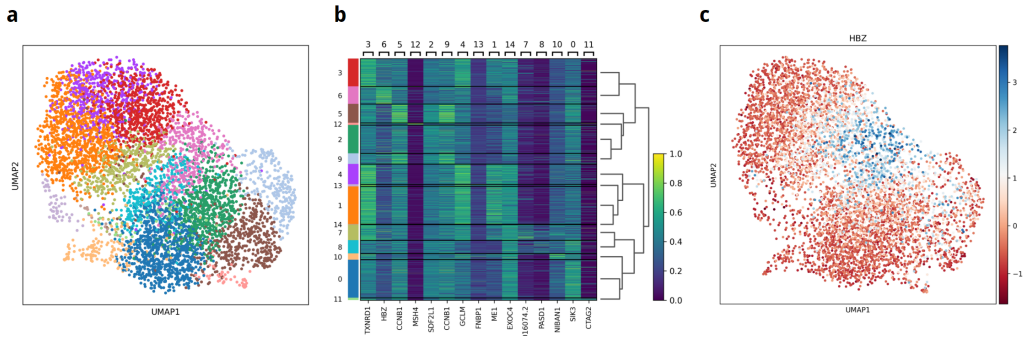

Figure 5.6: Screen-seq compatibility with commercial scRNA-seq. (a) K562 cells were encapsulated in droplets with barcode conjugates through the Screen-seq chip. These cells were incubated for 20 hours and then recovered with an optimized droplet lysis protocol. Profiling of the recovered cells with 10X Genomics scRNA-seq revealed 5,808 high-quality cells, which clustered together into 15 groups based on expression heterogeneity. Shown is a UMAP projection of the recovered cells, colored by cluster. (b) Heatmap of the top overexpressed genes that defined each cluster. (c) The gene coding for the hemoglobin-zeta subunit (HBZ) was differentially expressed across the sample, matching results from the literature [24–26]. Shown is the UMAP projection from (a), colored by level of HBZ expression.

the integration of the Screen-seq protocol with established commercial scRNA-seq pipelines.

5.4.3 Screen-seq decodes cell conditions alongside the transcriptome

A sequencing-based validation experiment was designed and carried out to confirm that droplet contents can indeed be decoded with the Screen-seq barcoding strategy. K562 cells were connected to the chip alongside 8 prepared barcodes dissolved in PBS. The chip was programmed to make droplets that only contained specific subsets of the possible barcode combinations. Two of the eight barcodes were assigned to be added to droplets with mutual exclusion (referred to as *Mono A* and *Mono B*). Another two barcodes were assigned to always be added into droplets together (*Pair-1* and *Pair-2*). Three other barcodes were assigned to always be added to droplets together (*Triple-1*, *Triple-2*, and *Triple-3*). One additional barcode was assigned to again be added only in isolation, however these droplets

were programmed to not be discarded during the transition window, in order to further evaluate the performance of the sorting strategy (*No-discard*). Clustering the sequencing results for this experiment based on barcode abundance revealed 5 distinct populations of cells (Figure 5.7a). One of the clusters corresponded to cells with high levels of the *Mono A* barcode, and a second, separate, cluster corresponded to cells with high levels of the *Mono B* barcode (Figure 5.7b). Conversely, a third cluster corresponded to cells that had high levels of both the *Pair-1* and *Pair-2* barcodes, demonstrating that the barcoding strategy can be used to identify cells that received distinct reagents or a combination of reagents (Figure 5.7c). Furthermore, a fourth cluster corresponded to cells that simultaneously had high levels of the *Triple-1*, *Triple-2*, and *Triple-3* barcodes, which supports the use of the Screen-seq screening platform beyond pairs of reagents (Figure 5.7d). The final cluster was observed to have varying amounts of the *No-discard* barcode, with a large number of cells that did not have any of the 8 barcodes (negative controls)(Figure 5.7e). This observation confirms the importance of the sorting strategy to discard droplets during the transition window, which will prevent a reagent from clustering with its negative control. Lastly, hierarchical clustering of cells and barcodes indeed grouped *Pair-1* and *Pair-2* together, as well as *Triple-1*, *Triple-2*, and *Triple-3* (Figure 5.8). These results together validate the Screen-seq barcoding strategy for decoding droplet conditions through sequencing.

5.4.4 A preliminary screen of chemotherapy drug combinations

Eight chemotherapy drugs (cytarabine, dasatinib, imatinib, homoharringtonine, hydroxyurea, ruxolitinib, tanespimycin, and vorinostat) were selected for combinatorial screening against the K562 cell line. This drug set interacts with multiple molecular pathways, from protein folding to nucleotide recycling. The Screen-seq chip was programmed to screen all 256 possible combinations of the 8 reagents in droplets of K562 cells, which were then incubated off-chip for 20 hours. Drug concentrations were chosen to be below the EC50 for each

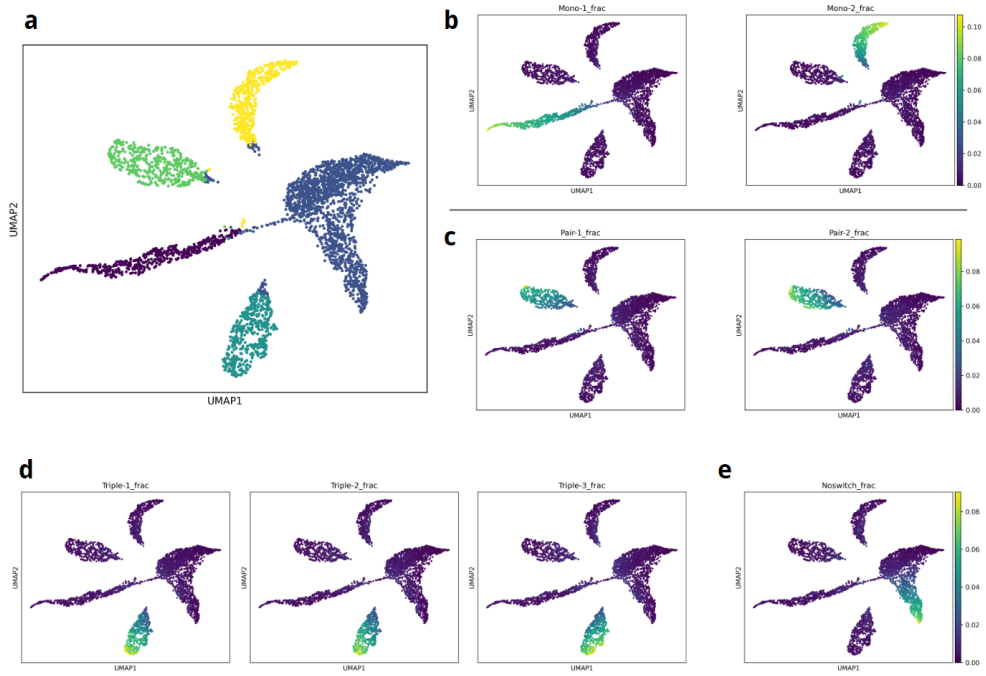

Figure 5.7: Sequencing validation of the Screen-seq platform. (a) K562 cells were treated with the Screen-seq protocol. The device was programmed to expose cells to five distinct combinatorial subsets of 8 barcoded tubes of PBS. Shown is a UMAP projection of the captured cells based on the detected amount of Screen-seq barcodes. (b) Two barcodes were programmed to be administered with mutual exclusion. Shown are two instances of the UMAP projection from (a), respectively colored by each of the barcodes. Barcodes were separately observed in two distinct clusters. (c) Two barcodes were programmed to be administered together. These were correctly detected at high levels in the same cluster of cells. (d) Three barcodes were programmed to be administered together. Again, these were correctly seen in the same cell cluster. (e) One additional barcode was programmed to be administered in isolation, however without use of the droplet sorting strategy to discard transitioning droplets. This barcode appeared to cluster with control droplets, highlighting the importance of discarding to improve separation of distinct conditions.

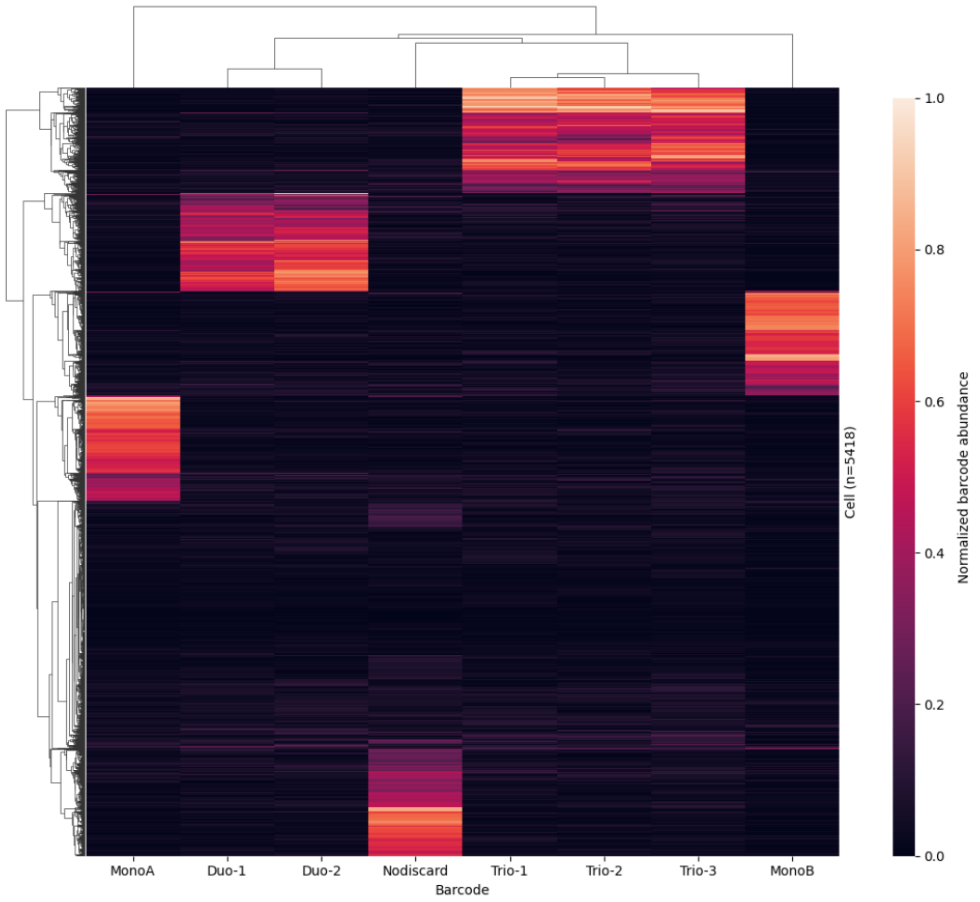

Figure 5.8: Hierarchical clustering of sequencing validation. K562 cells from the sequencing validation experiment were computationally clustered together based on barcode abundance. The barcodes were also clustered together based on similarity of cell populations. The barcodes that were administered in tandem were observed to cluster together, while barcodes administered with mutual exclusion clustered separately.

drug based on a 20-hour well plate experiment.

10X scRNA-seq identified 3,654 high-quality cells in the recovered sample with 10 clusters of transcriptomic heterogeneity. Clustering cells by barcode revealed distinct populations that corresponded to high- and low- levels of six of the tested drugs. Cells were not observed that contained high levels of either omacetaxine or vorinostat. A handful of genes showed statistically significant differential expression across treatment conditions, such as upregulation of the TGF-β pathway with tanespimycin, however the separation of responses for cells incubated with the chosen drug concentrations and duration was difficult to qualitatively appreciate. Nevertheless, this preliminary example serves as an important optimization step to further tune the platform for cancer drug screening.

5.5 Discussion and Future Directions

The Screen-seq platform is a powerful tool to measure the effects that different combinations of reagents will have on the transcriptome of single cells. By integrating microfluidic valves into a droplet generation device, a high level of both throughput and control can be achieved. Molecular barcoding labels each cell based on the contents of the droplet, so that the chemical composition can be decoded through standard scRNA-seq pipelines. The platform was evaluated with fluorochrome dyes to confirm the accuracy of programmed conditions and validated with sequencing to assess the fidelity of the encoding strategy.

A preliminary drug screening experiment was carried out on the platform with combinations of 8 chemotherapy drugs. While the molecular barcodes were indeed retained on cells and formed treatment clusters, the observed transcriptomic responses were underwhelming. Furthermore, the protocol failed to capture populations of cells that were exposed to two of the eight drugs, which could be due to a number of factors. One possibility is that the concentration used for these drugs was excessive for the incubation time: cells that were exposed to vorinostat or omacetaxine died before recovery, and were either chemically or computa-

tionally excluded from further analysis. Conversely, the weak transcriptomic responses to other drugs may have been due to insufficient concentrations or suboptimal duration of incubation. Transcriptomic responses can be comparatively quick, on the order of a few hours [27], which could be missed with a 20-hour endpoint. This experiment could be performed several times to hone in on the optimal concentrations and incubation conditions, however this runs contrary to the high-throughput premise of the Screen-seq platform.

Screen-seq can be improved with additional methods to capture cell responses to different concentrations of a reagent. Pulse-width modulation is a method used in electronics and communications to control the time-averaged strength of a signal with a two-state controller [28], and can be applied to valve-based microfluidic devices to produce reagent flows at intermediate concentrations [29]. In the Screen-seq chip, the reagent/vehicle valve pairs can be alternately actuated at a frequency much higher than the transition window. As the frequency increases, the concentration of the reagent at the droplet generation junction will approach a 50% steady-state value. By varying the duty cycle of the alternating valve actuation, this steady-state value can be precisely adjusted to select a specific concentration for droplet generation. The concentration of each reagent in the droplet is already encoded by the current barcoding strategy, however the noise of this signal will limit the resolution of measurement. The barcoding schema can be modified to instead use a unique barcode for each vehicle, which may improve the resolution.

Supplementary barcodes can also be used to capture responses of cells sampled at different time points [30]. Each sample can be labeled with a unique hashtag oligonucleotide, either before droplet encapsulation or prior to scRNA-seq, and pooled together for multiplexed analysis in one experiment. This approach is commonly used in single-cell analysis to produce "pseudotime" trajectories that link snapshot measurements of different, but correlated, cell populations together [30, 31]. Integration of time-resolved barcoding and pseudotime analysis into the Screen-seq platform can capture both short- and long-term transcriptomic responses

at once.

Screen-seq was initially designed with cancer drug screening in mind, however the technology can be more broadly applied to investigate other diseases and biological systems. Immune cells can be incubated with various combinations of cytokines to understand how complex chemical environments can be sensed and internally modeled by cellular pathways. Signaling molecules and hormones can be screened on stem cells to find combinations that drive differentiation along desired paths. The microfluidic and molecular platform discussed in this chapter has been validated for broad applications in high-throughput reagent screening, and there are many possibilities. Screen-seq serves as an important step towards improving the throughput and capabilities of single-cell analysis.

5.6 Methods

5.6.1 Device design and fabrication

The Screen-seq microfluidic chip was designed with AutoCAD software (Autodesk) and fabricated with standard soft lithography protocols. Briefly, molds for each device were produced on silicon wafers with SU-8 3025 (Kayaku) and AZ 40XT (Microchemicals) photoresists. The AZ photoresist was used to produce rounded feature cross-sections at valve junctions, through overnight reflow at 200C, to ensure that channels are completely sealed. The molds were used to embed the design for the control and flow layers in polydimethylsiloxane (PDMS). The control and flow layers were bonded together and to glass with a plasma cleaner (Harrick) under pure oxygen and at high power for 25 seconds. Finally, the device fluid channels were rendered superhydrophobic with Aquapel, flushed with air, and baked overnight.

5.6.2 Chip operation

All fluidic reagents were dispensed and prepared in 2 mL microcentrifuge tubes with membrane caps (Sarstedt). Tubes were connected to the Screen-seq device via Tygon microbore tubing and blunt needles. A digital pressure controller (Elveflow OB1) was used to independently set the pressures for the oil (BioRad Droplet Generation Oil for EvaGreen) and cell sample tubes, as well as a 16-plex tubing manifold connected to all screening reagents and vehicle controls. The microfluidic valves were controlled via external electronic solenoids assembled on a custom structural rig and connected via Tygon tubing. The solenoids in turn were actuated by a USB microcontroller (Elexol), which was programmed through custom Python software.

5.6.3 Fluorescence validation

Fluorescein sodium salt (Sigma) and resorufin sodium salt (Cayman Chemical) were used to quantitatively measure the controlled droplet generation process. Droplets were collected in a microcentrifuge tube and imaged in a monolayer on a hemocytometer (Neubauer) with a fluorescence microscope (Nikon). A simple image segmentation pipeline was written in Python to detect each circular droplet in brightfield images, and the corresponding pixels in the fluorescence channels were summed together to quantify the concentration of fluorochrome in each droplet.

5.6.4 Barcode synthesis

Anti-CD298 antibodies were purchased from BioLegend and functionalized with dibenzocyclooctyne (DBCO) groups with an amine-reactive NHS ester (DBCO-PEG4-NHS ester, Click Chemistry Tools). A NanoDrop spectrophotometer was used to measure the average number of DBCO groups added per antibody (5.18). Antibodies were conjugated to Cy5 through copper-free click chemistry (Cy5-azide, Click Chemistry Tools) for flow cytometry.

17 oligonucleotides were purchased from IDT with azide functionalization of the 5' end. The oligonucleotides contained regions for hybidization of Illumina TruSeq Read 2 primer and 10X Capture Sequence 1. Each oligonucleotide contained a 15-bp barcode sequence and was selected to be a Hamming distance of at least 7 bases apart.

5.6.5 Cell culture

K562 cells were obtained from ATCC and cultured in Iscove's Modified Dulbecco's Medium (IMDM) supplemented with 10% (v/v) fetal bovine serum. Subculturing was performed every 3 days to maintain cell density between $1x10^5$ and $1x10^6$ cells per mL.

5.6.6 Sample and reagent preparation

OptiPrep gradient density media (Sigma) was used to prepare all reagents at 16% (v/v) in complete IMDM. For screening, cells were counted and resuspended in the density-matched media at $1x10^6$ cells per mL. Barcodes were diluted to 10 nM in density-matched media. Chemotherapy drugs (cytarabine, dasatinib, imatinib, homoharringtonine, hydroxyurea, ruxolitinib, tanespimycin, and vorinostat) were purchased from Cayman Chemical and resuspended to 1 mg/mL in DMSO or PBS. Drugs were then further diluted in PBS to 0.1-1 µg/mL.

5.6.7 Droplet incubation and lysis

Droplets were collected in a microcentrifuge tube and incubated at 37C for 12-24 hours. For droplet lysis, the bottom layer of oil was first removed with a micropipette. An equivalent volume of perfluorooctanol (PFO, Sigma) was added along the walls of the tube and dropped through the emulsion layer to the bottom of the tube. The tube was then tilted 45 degrees and rotated about its long axis for 30 seconds to encourage droplet coalescence. The tube was then centrifuged at 100 x g for 10 seconds to completely separate the PFO and media

layers. The PFO was then removed with a micropipette and the aqueous (cell-containing) remainder was transferred to a 5 mL Falcon tube containing 2 mL of PBS + 1% BSA. Cells were washed twice with additional PBS + 1% BSA and then resuspended in PBS + 0.04% BSA.

5.6.8 Single-cell sequencing

scRNA-seq was performed according to the 10X Genomics protocol for Chromium Next GEM Single Cell 3' Reagent Kit v3.1 (Dual Index) with Feature Barcode technology for Cell Surface Protein. The protocol instructions were followed with the recovered cells to produce two separate DNA libraries for reverse-transcribed mRNA and captured Screen-seq barcodes. A NextSeq 2000 Sequencing System (Illumina) was used to sequence the DNA libraries: a P1 reagent cartridge and flow cell were used for the Screen-seq barcodes and a P2 reagent cartridge were used for cDNA. PhiX spike-ins were added to the barcode and cDNA samples at 1% and 40%, respectively, to maintain nucleotide diversity during sequencing.

5.6.9 Data analysis

Sequencing FASTQ files were uploaded to the 10X Genomics Cloud Analysis system. This tool runs the 10X Genomics *cellranger* pipeline on a computer cluster to align RNA reads to the genome a produce a gene expression matrix for the cells in the sample. The *scanpy* Python library [32] was used for quality control of the scRNA-seq data as well as clustering with the Leiden algorithm [33]. Seaborn [34] was used for all data visualization.

5.7 References

1. Brooks, M. D., Burness, M. L. & Wicha, M. S. Therapeutic Implications of Cellular Heterogeneity and Plasticity in Breast Cancer. en. *Cell Stem Cell* **17,** 260–271. ISSN:

1934-5909. https://www.sciencedirect.com/science/article/pii/S1934590915003690 (2023) (Sept. 2015).

2. Altschuler, S. J. & Wu, L. F. Cellular Heterogeneity: Do Differences Make a Difference? en. *Cell* **141,** 559–563. ISSN: 0092-8674. https://www.sciencedirect.com/science/article/pii/S0092867410004873 (2023) (May 2010).

3. Mokhtari, R. B. *et al.* Combination therapy in combating cancer. *Oncotarget* **8,** 38022–38043. ISSN: 1949-2553. https://www.ncbi.nlm.nih.gov/pmc/articles/PMC5514969/ (2023) (Mar. 2017).

4. Al-Lazikani, B., Banerji, U. & Workman, P. Combinatorial drug therapy for cancer in the post-genomic era. en. *Nature Biotechnology* **30.** Number: 7 Publisher: Nature Publishing Group, 679–692. ISSN: 1546-1696. https://www.nature.com/articles/nbt.2284 (2023) (July 2012).

5. Johnson, J. I. *et al.* Relationships between drug activity in NCI preclinical in vitro and in vivo models and early clinical trials. en. *British Journal of Cancer* **84.** Number: 10 Publisher: Nature Publishing Group, 1424–1431. ISSN: 1532-1827. https://www.nature.com/articles/6691796 (2023) (May 2001).

6. Cortazar, P. & Johnson, B. E. Review of the Efficacy of Individualized Chemotherapy Selected by In Vitro Drug Sensitivity Testing for Patients With Cancer. en. *Journal of Clinical Oncology* **17.** Publisher: American Society of Clinical Oncology, 1625–1625. ISSN: 0732-183X, 1527-7755. http://jco.ascopubs.org/content/17/5/1625 (2023) (May 1999).

7. Roda, A., Guardigli, M., Pasini, P. & Mirasoli, M. Bioluminescence and chemiluminescence in drug screening. en. *Analytical and Bioanalytical Chemistry* **377,** 826–833. ISSN: 1618-2650. https://doi.org/10.1007/s00216-003-2096-6 (2023) (Nov. 2003).

8. Zheng, W., Thorne, N. & McKew, J. C. Phenotypic screens as a renewed approach for drug discovery. en. *Drug Discovery Today* **18,** 1067–1073. ISSN: 1359-6446. https://www.sciencedirect.com/science/article/pii/S135964461300202X (2023) (Nov. 2013).

9. Vega-Avila, E. & Pugsley, M. K. An overview of colorimetric assay methods used to assess survival or proliferation of mammalian cells. eng. *Proceedings of the Western Pharmacology Society* **54,** 10–14. ISSN: 0083-8969 (2011).

10. Levitin, H. M., Yuan, J. & Sims, P. A. Single-Cell Transcriptomic Analysis of Tumor Heterogeneity. en. *Trends in Cancer. Special Issue: Physical Sciences in Oncology* **4,** 264–268. ISSN: 2405-8033. https://www.sciencedirect.com/science/article/pii/S2405803318300384 (2023) (Apr. 2018).

11. Liu, S. & Trapnell, C. Single-cell transcriptome sequencing: recent advances and remaining challenges. *F1000Research* **5,** F1000 Faculty Rev–182. ISSN: 2046-1402. https://www.ncbi.nlm.nih.gov/pmc/articles/PMC4758375/ (2023) (Feb. 2016).

12. Tang, F., Lao, K. & Surani, M. A. Development and applications of single-cell transcriptome analysis. en. *Nature Methods* **8.** Number: 4 Publisher: Nature Publishing Group, S6–S11. ISSN: 1548-7105. https://www.nature.com/articles/nmeth.1557 (2023) (Apr. 2011).

13. Macosko, E. Z. *et al.* Highly Parallel Genome-wide Expression Profiling of Individual Cells Using Nanoliter Droplets. en. *Cell* **161,** 1202–1214. ISSN: 0092-8674. https://www.sciencedirect.com/science/article/pii/S0092867415005498 (2023) (May 2015).

14. Zilionis, R. *et al.* Single-cell barcoding and sequencing using droplet microfluidics. en. *Nature Protocols* **12.** Number: 1 Publisher: Nature Publishing Group, 44–73. ISSN: 1750-2799. https://www.nature.com/articles/nprot.2016.154 (2023) (Jan. 2017).

15. Mathur, L. *et al.* Combi-seq for multiplexed transcriptome-based profiling of drug combinations using deterministic barcoding in single-cell droplets. en. *Nature Communications* **13.** Number: 1 Publisher: Nature Publishing Group, 4450. ISSN: 2041-1723. https://www.nature.com/articles/s41467-022-32197-0 (2023) (Aug. 2022).

16. Reyes, M., Leff, S. M., Gentili, M., Hacohen, N. & Blainey, P. C. Microscale combinatorial stimulation of human myeloid cells reveals inflammatory priming by viral ligands. *Science Advances* **9.** Publisher: American Association for the Advancement of Science, eade5090. https://www.science.org/doi/10.1126/sciadv.ade5090 (2023) (Feb. 2023).

17. Unger, M. A., Chou, H.-P., Thorsen, T., Scherer, A. & Quake, S. R. Monolithic Microfabricated Valves and Pumps by Multilayer Soft Lithography. *Science* **288.** Publisher: American Association for the Advancement of Science, 113–116. https://www.science.org/doi/full/10.1126/science.288.5463.113 (2023) (Apr. 2000).

18. Melin, J. & Quake, S. R. Microfluidic Large-Scale Integration: The Evolution of Design Rules for Biological Automation. *Annual Review of Biophysics and Biomolecular Structure* **36.** _eprint: https://doi.org/10.1146/annurev.biophys.36.040306.132646, 213–231. https://doi.org/10.1146/annurev.biophys.36.040306.132646 (2023) (2007).

19. Beard, D. A. Taylor dispersion of a solute in a microfluidic channel. *Journal of Applied Physics* **89,** 4667–4669. ISSN: 0021-8979. https://doi.org/10.1063/1.1357462 (2023) (Apr. 2001).

20. Stoeckius, M. *et al.* Cell Hashing with barcoded antibodies enables multiplexing and doublet detection for single cell genomics. *Genome Biology* **19,** 224. ISSN: 1474-760X. https://doi.org/10.1186/s13059-018-1603-1 (2023) (Dec. 2018).

21. Mazutis, L. *et al.* Single-cell analysis and sorting using droplet-based microfluidics. en. *Nature Protocols* **8.** Number: 5 Publisher: Nature Publishing Group, 870–891. ISSN: 1750-2799. https://www.nature.com/articles/nprot.2013.046 (2023) (May 2013).

22. Skhiri, Y. *et al.* Dynamics of molecular transport by surfactants in emulsions. en. *Soft Matter* **8,** 10618. ISSN: 1744-683X, 1744-6848. http://xlink.rsc.org/?DOI=c2sm25934f (2023) (2012).

23. Gruner, P. *et al.* Controlling molecular transport in minimal emulsions. en. *Nature Communications* **7,** 10392. ISSN: 2041-1723. https://www.nature.com/articles/ncomms10392 (2023) (Jan. 2016).

24. Rutherford, T. *et al.* Embryonic erythroid differentiation in the human leukemic cell line K562. *Proceedings of the National Academy of Sciences* **78.** Publisher: Proceedings of the National Academy of Sciences, 348–352. https://www.pnas.org/doi/abs/10.1073/pnas.78.1.348 (2023) (Jan. 1981).

25. Testa, U. *et al.* Hemoglobin Expression in Clones of K562 Cell Line. en. *European Journal of Biochemistry* **121.** _eprint: https://onlinelibrary.wiley.com/doi/pdf/10.1111/j.1432-1033.1982.tb05835.x, 649–655. ISSN: 1432-1033. https://onlinelibrary.wiley.com/doi/abs/10.1111/j.1432-1033.1982.tb05835.x (2023) (1982).

26. Rowley, P. T., Ohlsson-Wilhelm, B. M., Wisniewski, L., Lozzio, C. B. & Lozzio, B. B. K562 human leukemia cell passages differ in embryonic globin gene expression. en. *Leukemia Research* **8,** 45–54. ISSN: 0145-2126. https://www.sciencedirect.com/science/article/pii/0145212684900304 (2023) (Jan. 1984).

27. Tay, S. *et al.* Single-cell NF-KB dynamics reveal digital activation and analogue information processing. en. *Nature* **466.** Number: 7303 Publisher: Nature Publishing Group, 267–271. ISSN: 1476-4687. https://www.nature.com/articles/nature09145 (2023) (July 2010).

28. Sun, J. en. in *Dynamics and Control of Switched Electronic Systems: Advanced Perspectives for Modeling, Simulation and Control of Power Converters* (eds Vasca, F. & Iannelli, L.) 25–61 (Springer, London, 2012). ISBN: 978-1-4471-2885-4. https://doi.org/10.1007/978-1-4471-2885-4_2 (2023).

29. Ainla, A., Gözen, I., Orwar, O. & Jesorka, A. A Microfluidic Diluter Based on Pulse Width Flow Modulation. *Analytical Chemistry* **81.** Publisher: American Chemical Society, 5549–5556. ISSN: 0003-2700. https://doi.org/10.1021/ac9010028 (2023) (July 2009).

30. Kim, H.-J. *et al.* Nuclear oligo hashing improves differential analysis of single-cell RNA-seq. en. *Nature Communications* **13.** Number: 1 Publisher: Nature Publishing Group, 2666. ISSN: 2041-1723. https://www.nature.com/articles/s41467-022-30309-4 (2023) (May 2022).

31. Ji, Z. & Ji, H. TSCAN: Pseudo-time reconstruction and evaluation in single-cell RNA-seq analysis. *Nucleic Acids Research* **44,** e117. ISSN: 0305-1048. https://doi.org/10.1093/nar/gkw430 (2023) (July 2016).

32. Wolf, F. A., Angerer, P. & Theis, F. J. SCANPY: large-scale single-cell gene expression data analysis. en. *Genome Biology* **19,** 15. ISSN: 1474-760X. https://genomebiology.biomedcentral.com/articles/10.1186/s13059-017-1382-0 (2023) (Dec. 2018).

33. Traag, V. A., Waltman, L. & van Eck, N. J. From Louvain to Leiden: guaranteeing well-connected communities. en. *Scientific Reports* **9.** Number: 1 Publisher: Nature Publishing Group, 5233. ISSN: 2045-2322. https://www.nature.com/articles/s41598-019-41695-z (2023) (Mar. 2019).

34. Waskom, M. seaborn: statistical data visualization. *Journal of Open Source Software* **6,** 3021. ISSN: 2475-9066. https://joss.theoj.org/papers/10.21105/joss.03021 (2023) (Apr. 2021).

CHAPTER 6

CONTRIBUTIONS AND OUTLOOK

Drug screening systems can help comb through the space of treatment possibilities to find promising options for clinical studies. This strategy is especially important for cancer treatment, as there is a large number of drugs that may be effective in different cases. The research contributed in this dissertation focused on working with drug screening systems to improve the number of testable conditions (throughput) and the richness of measurement outputs (content).

OrganoID automates the image analysis process for organoid experiments, which can be a key bottleneck for throughput. The software tool was used to measure detailed morphological responses, which uncovered changes in the shape and size of pancreatic cancer organoids with the addition of a chemotherapy drug. Organoids can be tracked over time, through brightfield microscopy, without the need for fluorescent dyes or genetically engineered fusion proteins.

PicoScreen brought the focus to the microfluidic level with a novel device strategy for drug screening. Multiplexed membrane valves and droplet microfluidic geometry were combined into a single device to produce droplets with controllable chemical compositions. The droplets were then stored on-chip in an ordered array, so that responses can be followed with microscopy over time. PicoScreen was tested with food dye for qualitative validation, which supported further development. This tool can have many exciting applications in both biological and cell-free systems, such as cancer drug screening, antibiotic resistance screening, bacteriophage screening, or optimization of protein crystallization conditions.

Screen-seq adapted the microfluidic schema from PicoScreen to instead uncover changes in cellular transcriptomes in response to different combinations of reagents. The microfluidic chip was designed such that each droplet was paired with the appropriate negative control and contained the specifically programmed chemical composition with additional sorting valves. Antibody-olignucleotide conjugates were synthesized to encode the droplet contents on each

cell, which could be measured and decoded alongside the transcriptome through commercial single-cell RNA seqeuencing. This system was validated extensively with both fluorophores and a sequencing experiment, and was preliminarily explored to screen combinations of cancer drugs, which identified important future directions for the project.

These works are considerable contributions to the field of high-throughput screening. Microfluidic, computational, and molecular strategies can be used to supplement existing platforms, so that more conditions can be screened in tandem, more efficiently, and with more information-rich measurements. Through further development and exploration, OrganoID, PicoScreen, and Screen-seq will play central roles in the effort to more comprehensively and expediently investigate biological and biochemical phenomena, so that disease processes, such as cancer, can be more thoroughly understood and effectively treated for each and every patient.